

Mapping of magnetospheric electric fields from Cluster into ionospheric convection from SuperDARN using the Tsyganenko field model.

by

Fulufhelo Kenneth Maphaha

A thesis submitted in fulfilment of the academic requirements for the degree of Master of Science in the School of Physics, University of KwaZulu-Natal, Durban

December 2010

As the candidate's supervisor approve/do not approve this thesis for submission

Signed: Name: Date:

As the candidate's supervisor approve/do not approve this thesis for submission

Signed: Name: Date:

Abstract

The data from Super Dual Auroral Radar Network (SuperDARN) radar and Cluster was used to investigate whether the processes observed by SuperDARN radar in the high-latitude ionosphere leads to the processes that take place in the magnetosphere. SuperDARN is a global network of high-frequency coherent-scatter radars operating in the northern and southern hemispheres and these radars are capable of observing backscatter from ionospheric irregularities. The Tsyganenko T96 field model was used to map the footprint of the Cluster spacecraft into the ionosphere. The SuperDARN radar data analysis software was used to generate time series, field of view and convection plots. The data from Syowa South, Syowa East SuperDARN radars, Advance Composition Explorer (ACE) and Cluster spacecrafts was used in this study. Two events were found and discussed, an event on 09 August 2002 and another event on 30 September 2002. The SuperDARN radar and Cluster data for these events were compared. When a change in electric field was observed by Cluster, SuperDARN radar observed a change in the convection flow. There was a time delay between the change in the electric field and the change in convection flow.

PREFACE

The experimental work described in this MSc dissertation was carried out at the Hermanus Magnetic Observatory, Hermanus and the School of Physics, University of KwaZulu-Natal, Durban, from February 2008 to December 2009 under the supervision of Prof. Sadha Pillay and Dr Lindsay Magnus.

These studies represent original work by the author and have not otherwise been submitted in any form for any degree or diploma to any tertiary institution. Where the work of others was used, it was duly acknowledged in the text.

Fulufhelo Kenneth Maphaha

DECLARATION 1 - PLAGIARISM

I, declare that

1. The research reported in this thesis, except where otherwise indicated, is my original research.
2. This thesis has not been submitted for any degree or examination at any other university.
3. This thesis does not contain another person's data, pictures, graphs or other information, unless specifically acknowledged as being sourced from other persons.
4. This thesis does not contain another person's writings, unless specifically acknowledged as being sourced from other researchers. When other written sources have been quoted, then:
 - (a) Their words have been re-written, but general information attributed to them has been referenced
 - (b) Where their exact words have been used, their writing has been placed in italics and inside quotation marks, and referenced
5. This thesis does not contain text, graphics or tables copied and pasted from internet, unless specifically acknowledged, and the source detailed in the thesis and in the reference sections.

Signed:

DECLARATION 2 - PUBLICATIONS

DETAILS OF THE CONTRIBUTORS TO PUBLICATIONS that form part of and/or include research presented in this thesis. Include publications in preparation, submitted, *in press* and published. Give details of the contribution of each author to the experimental work and writing of each publication.

Publication 1

Publication 2

Publication 3

etc.

Signed:

Acknowledgements

I would like humbly thank and acknowledge the following for their contribution to the success of this study:

- My supervisors, Dr Lindsay Magnus and Prof. Sadha Pillay for their help and guidance throughout this study.
- Mr Sibusiso Mthembu, Mr Dzivhuluwani Ndiitwani, Dr Patrick Sibanda and Dr Jim Wild for their assistance.
- Hermanus Magnetic Observatory (HMO) for financial assistance and accommodation for the duration of the study.
- National Institute of Polar Research, Syowa South and Syowa East SuperDARN radars for HF data.
- Johns Hopkins University Applied Physics Laboratory for SuperDARN toolkit (data analysis software).
- Dr Ron Barnes for the development of SuperDARN toolkit.
- D.J McComas of Southwest Research Institute for providing ACE interplanetary magnetic field and solar-wind data.
- Cluster Science Data System (CSDS) and Dr L.P. Lindqvist for validating and making the Cluster EFW data available.
- Haje Korth of JHU/APL for the IDL geopack DLM (Tsyganenko field model) which was used in this study.
- Munzhedzi and my family for making everything better.
- MaCele for the support, courage and love she showed when things looks tough.
- Mr Mudau for making physical science easier during my secondary school days.
- Mr Obed Shirinda, Ms Elda Saunderson and Ms Jean Pierre for proof reading this work.
- Friends inside and outside HMO.

Dedication

To Munzhedzi

Contents

1	Introduction	1
1.1	Project objectives	1
1.2	Thesis overview	1
2	The Magnetosphere and magnetospheric convection	3
2.1	The solar wind and the interplanetary magnetic field (IMF)	3
2.2	The magnetosphere	4
2.2.1	The Bow shock	4
2.2.2	Magnetopause	4
2.2.3	The Magnetotail	5
2.2.4	The Plasmasphere	6
2.3	The Ionosphere	6
2.4	The open-closed boundary	7
2.5	The Magnetosphere and Ionosphere convection	8
2.5.1	Dependencies of convection	9
2.5.2	Interplanetary magnetic field dependencies	9
2.5.3	Seasonal dependencies	11
2.6	Magnetic field models	12
2.7	The internal field model	13
2.7.1	Spherical harmonic representation of the main field	13
2.8	The external field model	14
2.8.1	The Tsyganenko T96 field model	14
2.8.2	Field line trace	15
2.8.3	Footprint plots	17
2.9	Conclusion	17

3	Instruments and data format	19
3.1	Super Dual Auroral Radar Network (SuperDARN)	19
3.2	The Cluster satellite	23
3.2.1	Electric Field and Wave (EFW) instrument	25
3.3	The Advanced Composition Explorer (ACE) satellite	25
3.4	Conclusion	28
4	Survey of Cluster and SuperDARN radar successes	29
4.1	Successes using SuperDARN radar and Cluster data	29
4.1.1	Successes using SuperDARN radar data	30
4.1.2	Successes using Cluster data	31
4.2	Conclusion	31
5	Data analysis techniques	33
5.1	SuperDARN data analysis software	33
5.1.1	Time series plots	33
5.1.2	Field of view plots	35
5.1.3	Convection plots	37
5.2	Convection map orientation	39
5.3	Conclusion	40
6	Results	41
6.1	Events observed on 09/08/2002	41
6.1.1	Observations by the Cluster satellite	42
6.1.2	Observations by the SuperDARN radar	45
6.1.3	Comparison of the Cluster and SuperDRN data	47
6.2	Events observed on 30/09/2002	47
6.2.1	Observations by the Cluster satellite	50
6.2.2	Observations by the SuperDARN radar	50
6.2.3	Comparison of the Cluster and SuperDRN data	52
6.3	Conclusion	53

7 Discussion and Conclusion	54
7.1 Future work	56
A SuperDARN data analysis software	57
A.1 SuperDARN data analysis software	57
A.1.1 Time series plots	57
A.1.2 Field of view plots	58
A.1.3 Convection plots	59
References	61

List of Figures

2.1	The structure and regions of the magnetosphere, [2].	5
2.2	The regions of the ionosphere and electron density profile, [27].	7
2.3	Open-closed field line boundary for $B_y = 5$ nT, $B_z = -5$ nT, $n = 5$ cm ⁻³ and $U = 300, 500$ and 800 km/s (left) and open-closed field line boundary for $B_y = 5$ nT, $B_z = 0$ nT, $n = 5$ cm ⁻³ , and $U = 300, 500,$ and 800 km/s (right). The solar wind dynamic pressure is the same, [15].	8
2.4	Statistical ionospheric convection patterns. The patterns depend on the IMF clock angle in the middle of the patterns, [28].	10
2.5	Statistical ionospheric convection patterns during the winter and summer seasons for predominantly IMF B_y+ . The magnitude of the magnetic field was 3-5 nT, [28].	11
2.6	Statistical ionospheric convection patterns during the winter and summer seasons for predominantly IMF B_y- . The magnitude of the magnetic field was 5-10 nT, [28].	12
2.7	The noon-midnight projection of geomagnetic field lines during strong northward directed IMF. The solar wind dynamic pressure (P_{dyn}) = 2.5 nPa, IMF $B_y = 4.0$ nT and $B_z = +10.7$ nT, [32].	15
2.8	Field line trace from space to northern hemisphere (left) and field line trace from spacecraft to southern hemisphere (right). The field lines were traced with the Tsyganenko T96 field model.	16
2.9	Spacecraft's magnetic footprint mapped using the Tsyganenko T96 field model. The green stars represent footprint, red numbers represent universal time (UT) in hours and the triangles represent the field of view of SuperDARN radar in the southern hemisphere.	17
3.1	SuperDARN radars in the northern hemisphere (left) and SuperDARN radars in the southern hemisphere (right).	20
3.2	SuperDARN antenna array at SANAE, Antarctica.	20

3.3	The HF signal transmitted by the radar to the ionosphere, [33].	21
3.4	The plot of backscatter power (top panel), the line of sight doppler velocity (middle panel) and spectral width (bottom panel). The plots were produced using SuperDARN data analysis software.	22
3.5	Cluster spacecraft orbit during the first year of the mission, [9].	24
3.6	Spacecraft configuration when the apogee is at local noon, local midnight and magnetotail, [9].	24
3.7	Interplanetary magnetic field measured by ACE spacecraft in Geocentric Solar Magnetic coordinates on 03-08-2004 for the time interval 00 to 00 UT. The plot was produce using SuperDARN data analysis software.	26
3.8	Solar wind velocity measured by ACE spacecraft in Geocentric Solar Magnetic coordinates on 03-08-2004 for the time interval 00 to 00 UT. The plot was produce using SuperDARN data analysis software.	27
5.1	Time series plot: backscatter power (top panel), the line of sight doppler velocity (middle panel) and spectral width (bottom panel). The plots were produced using SuperDARN data analysis software.	34
5.2	Field of view plots show the doppler velocity during the time period 07:01 - 07:05 UT. The plot was produced using SuperDARN data analysis software.	36
5.3	Procedure for generating time series and field of view plots	37
5.4	Procedure for generating convection maps	38
5.5	Convection map plot showing the convection during the time period 00:02 - 00:04 UT in the southern hemisphere. The plot was produced using SuperDARN data analysis software.	39
6.1	Spacecraft magnetic footprint mapped using the Tsyganenko T96 field model. The green stars represent the footprint position, red numbers give universal time (UT) in hours and the triangles represent the field of view of SuperDARN radar in the southern hemisphere.	42
6.2	The electric field measured by Cluster spacecrafts. The black plotrepresents from Cluster 1 (C1), the red plot represents Cluster 2 (C2), the green plot represents Cluster 3 (C3) and the blue plot represents Cluster 4 (C4). The plots are for the time interval 01:00 - 02:00 UT.	43
6.3	Interplanetary magnetic field measured by the ACE spacecraft in Geocentric Solar Magnetic coordinates on 09/08/2002 for the time interval 00 to 02 UT. The plot was produced using SuperDARN toolkit utility istp_plot.	44

6.4	Convection plots with 2-min intervals. The duskside is on the left, dawnside is on the right, noon at the bottom and midnight at the top. The plots show convection during 01:44 - 01:52 UT.	45
6.5	Convection plots with 2-min intervals. The duskside is on the left, dawnside is on the right, noon at the bottom and midnight at the top. The plots show convection during 01:52 - 02:00 UT.	46
6.6	Spacecraft magnetic footprint mapped using the Tsyganenko T96 field model. The green stars represent the footprint position, red numbers represent universal time (UT) in hours and the triangle represents the field of view of the SuperDARN radar in southern hemisphere.	48
6.7	Interplanetary magnetic field measured by ACE spacecraft in Geocentric Solar Magnetic coordinates on the 30-09-2002 for the time interval 20:00 - 22:00 UT. The plot was produce using SuperDARN toolkit utility istp_plot.	49
6.8	The electric field measured by the Cluster spacecrafts. The black plot represents from Cluster 1 (C1), red plot represents from Cluster 2 (C2), green plot represents from Cluster 3 (C3) and blue plot represents from Cluster 4 (C4).	50
6.9	Convection plots with 2-min intervals. The duskside is on the left, dawnside is on the right, noon at the bottom and midnight at the top. The plots represents convection during 21:12 - 21:18 UT.	51
6.10	Convection plots with 2 min intervals. The duskside is on the left, dawnside is on the right, noon at the bottom and midnight at the top. The plots represents convection during 21:21 - 21:28 UT.	52

List of Tables

6.1	The Tsyganenko field model parameters used to map the Cluster footprint on the 09 August 2002.	41
6.2	The Tsyganenko field model parameters used to map the Cluster footprint on the 30 September 2002.	48

Chapter 1

Introduction

This chapter defines the objectives of this study and gives an overview of the work that was done, chapter by chapter.

1.1 Project objectives

In this project we are investigating if the mapping of magnetospheric processes into the ionosphere can be used to confirm whether the processes observed by Super Dual Auroral Radar Network (SuperDARN) result from the processes taking place in the magnetosphere. This can be achieved by using magnetic field models (Tsyganenko T96 field model), satellite instruments (Cluster satellite) and ground-based instruments (SuperDARN radar). This project had the following objectives, namely:

- To understand the magnetosphere, ionospheric regions and electric field convection.
- To understand how the Tsyganenko field model works and be able to use it to map spacecrafts footprint into the ionosphere.
- To understand SuperDARN radar data and to use its data analysis software.
- To understand Cluster satellite data and the specific instrument that collects the electric field data.
- To compare data from Cluster satellites and ground-base SuperDARN radars.

1.2 Thesis overview

Chapter 2 focuses on the magnetospheric regions, and magnetospheric and ionospheric convections. The properties of the solar wind, open-closed field line boundary, magnetic field models, and convection and its dependencies are discussed.

In chapter 3 the SuperDARN radar, the Cluster and ACE spacecrafts are discussed. These are the main instruments used in this study. The chapter focuses on the location of the instruments and their operation. The parameters of interest and examples of the data plots are also discussed.

Chapter 4 gives an overview of research using data from the SuperDARN radar and the Cluster spacecraft.

Chapter 5 focuses on the SuperDARN data analysis software and how convection maps, time and field of view plots can be produced using the software.

Chapter 6 presents results obtained using the magnetic field model, SuperDARN radar data and Cluster data. The electric field from Cluster and convection flow observed by SuperDARN radar are compared.

Chapter 7 presents an overall discussion of the project and conclusions.

Chapter 2

The Magnetosphere and magnetospheric convection

In this chapter the different regions of the magnetosphere and ionosphere are discussed. The solar wind plays an important role in the changes that we observe in the magnetosphere and ionosphere. The properties of the solar wind will be discussed here. Since space-based and ground-based instruments were used, magnetic field models were required to map the events taking place in magnetosphere down into the ionosphere. The internal and the external magnetic field models will be discussed and the role they play. The magnetosphere and ionosphere electric field will also be discussed. The satellite in space measures the electric field in the magnetosphere and the changes in the electric field are compared with the changes in plasma drift observed in high-latitude ionosphere.

2.1 The solar wind and the interplanetary magnetic field (IMF)

The flow of solar plasma and a remnant of the solar magnetic field that is present throughout the interplanetary space is referred to as the solar wind [16]. The huge pressure difference between the solar corona and an interstellar space drives the plasma outward, despite the restraining influence of solar gravity. The solar wind travels at a supersonic speed of ~ 450 km/s caused by the supersonic expansion of the solar corona. Some properties of the solar wind observed at 1 AU near the Earth orbit are discussed in [16]. When the solar wind flows towards the Earth at a supersonic speed, it hits the Earth's magnetic field [16]. This results in a decrease of the speed of the solar wind and it forms a shock wave known as the bow shock (see figure 2.1). The solar wind carries the sun's magnetic field to the interplanetary space and this magnetic field is referred to as the interplanetary magnetic field (IMF) [27]. The interplanetary magnetic field plays an important role during solar wind and magnetospheric coupling (see section 2.5). The energetic particles carried

by the solar wind are transferred into the magnetosphere when the interplanetary magnetic field connects with the Earth's magnetic field [27].

2.2 The magnetosphere

The Earth's magnetic field extends into the surrounding space and it acts as a barrier preventing charged particles to enter into the Earth's surrounding space, forming what is known as the magnetosphere [27]. The structure of the magnetosphere is influenced by the solar wind and the magnetic field from sun [27]. Satellites and ground-based instruments have been used to study the structure and the shape of the magnetosphere [27].

The shape and size of the magnetosphere emanates from the balance between the solar wind dynamic pressure and the magnetic pressure of Earth's intrinsic magnetic field [27]. When the solar wind is flowing towards the Earth, the magnetic field facing the sun is compressed and the field on the side away from the sun stretches forming a long tail like a comet [27]. The side of the Earth facing the sun is called the dayside and the side facing away is called the nightside [27]. The magnetosphere structure and its regions are shown in figure 2.1. We will now discuss the different regions of the magnetosphere.

2.2.1 The Bow shock

The solar wind plasma flowing towards the Earth at supersonic speeds collides with Earth's magnetosphere and a shock wave known as the bow shock is formed. After the collision, the speed of the solar wind is reduced as it passes the bow shock and the plasma starts to move upstream. As the solar wind moves past the bow shock it continues to move with the same velocity and the heat is spread around the magnetosphere [27]. The bow shock is located on the Earth's dayside magnetosphere and some satellite observations have confirmed the presence of this shock wave (see figure 2.1). Some of the solar wind particles do not pass the bow shock, as they collide with bow shock are reflected backwards. The reflection of these particles is caused by the decrease in the solar wind velocity [27].

2.2.2 Magnetopause

The outer boundary of the magnetosphere that encloses the magnetic field lines extending from the Earth is called the magnetopause [27]. This boundary separates the geomagnetic field and the solar wind plasma originating from the sun (see figure 2.1). If the solar wind were not present, the geomagnetic field would extend from the Earth and completely fill the surrounding space [27]. When the solar wind is flowing at a supersonic speed towards the Earth, the geomagnetic fields facing the sun are compressed, forming a boundary layer (magnetopause). When the solar wind particles reaches the surface of the boundary they

get reflected, but they also exert pressure on the surface [27]. The location of the magnetopause can be calculated by making an assumption that the pressure in the magnetosphere is equal to the pressure in the magnetosheath [27].

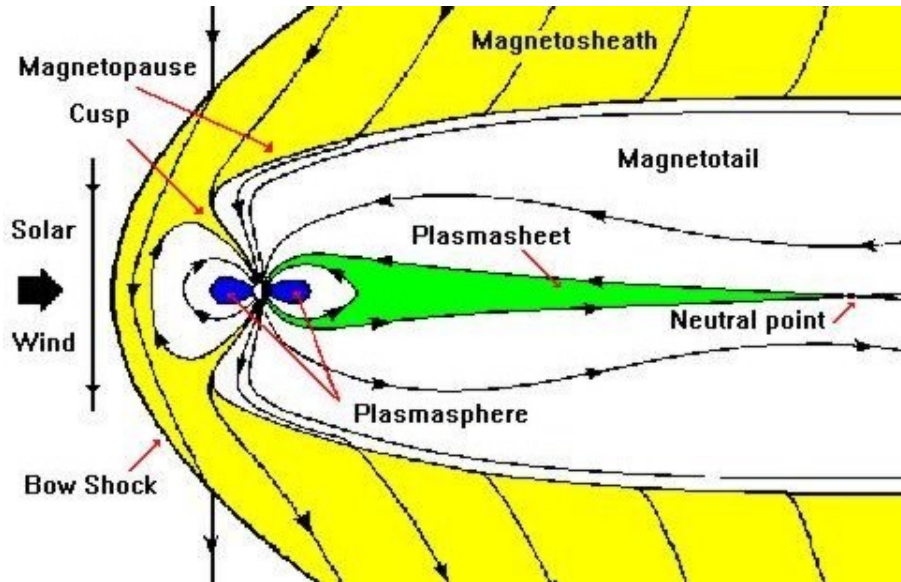


Figure 2.1: The structure and regions of the magnetosphere, [2].

2.2.3 The Magnetotail

The region of the Earth's magnetosphere that stretches away from the sun behind the Earth is referred to as the magnetotail [27]. This region is formed by one of two processes. (i) When the solar-wind dynamic pressure exerts pressure on the geomagnetic field. This results in the compression of the geomagnetic field on the side facing the sun (dayside) and the stretching of the geomagnetic field away from the Earth (nightside) forming what is called the magnetotail. (ii) The reconnection that occurs on the dayside magnetosphere. This results in the open field line of the force [27]. Due to the presence of the solar wind, the open field line will be blown to the nightside of Earth transporting the magnetic flux to the nightside where it is stored [27].

The magnetotail consists of the northern and the southern lobe. The magnetic field on the north side pointing towards the Earth is referred to as the north lobe and the magnetic field on the south side pointing away from the Earth is referred to as the south lobe (see figure 2.1). The lobes have a diameter of 40-50 R_E and the plasma density is extremely low [27].

The sheet structure with hot plasma in the equatorial region of the magnetotail is called the plasmasheet [27]. The magnetic field in this region is weak [27]. The ion average temperature in the plasmasheet is several thousand electron volts and the electron average temperature is hundred electron volts. The plasma that enters the plasmasheet is trapped since the field lines are closed and this results in an increase in density. The pressure

increases towards the centre, resulting in the electric current produced by the gradient pressure of plasma flowing in the plasma sheet [27]. for more details see [27].

2.2.4 The Plasmasphere

The region inside the plasmopause is called the plasmasphere and this region is considered as an extension of the ionosphere. The particles in the plasmasphere result from the diffusion of plasma from the ionosphere and these particles have low energies [27].

The shape of the plasmasphere depends on the electric field in the magnetosphere [27]. When the magnetosphere electric field increases, the plasmopause moves towards the Earth, which results in a decrease in plasmasphere. If the electric field of the magnetosphere is uniform, the plasmasphere will have a teardrop-like shape [27].

2.3 The Ionosphere

The upper ionised layer of the Earth's atmosphere is referred to as the ionosphere. The layer consists of ionised gases, electrons and ions as a result of the absorption of solar radiation. During the recombination process these ions and electrons combine and the neutral gases are formed. This layer plays an important role during high frequency radio wave propagation. This layer is capable of reflecting radio waves when entering the region with high electron density [27]. The ionosphere is divided into three different regions, namely, the D, E and F regions. The D region (70 ~ 100 km) is the region of low electron density and the electron density depends on the solar zenith angle. High electron density is observed in winter when the change in the solar zenith angle position is minimal [27]. In the E region (100 ~ 150 km) the electron density depends on the solar zenith angle and the ionisation in this region is caused by x-ray and far ultraviolet solar radiation of O_2 molecules. The E region is at maximum height at sunset and the refraction of HF radio wave increases. Since the sun disappears at night, the E region disappears because there is no source of radiation [27]. The F region (above 150 km), this is the upper region of the ionosphere where high ionisation takes place and the electron density is high compared to the other layers. The F region is divided into the F1 and F2 regions. F1 region is the region between 150 km and 250 km. This region appears in summer when the solar zenith angle and the ionisation angle are small. It appears during the solar minimum when the transition altitude is higher. The F2 region (above 250 km) is the uppermost region of the ionosphere and the ionisation in this region increases with the increase in altitude. At heights above 300 km the ionisation and electron density decreases as the height increases [27]. The electron density in all the ionospheric regions are higher during the day compared to the electron density at the night (see figure 2.2).

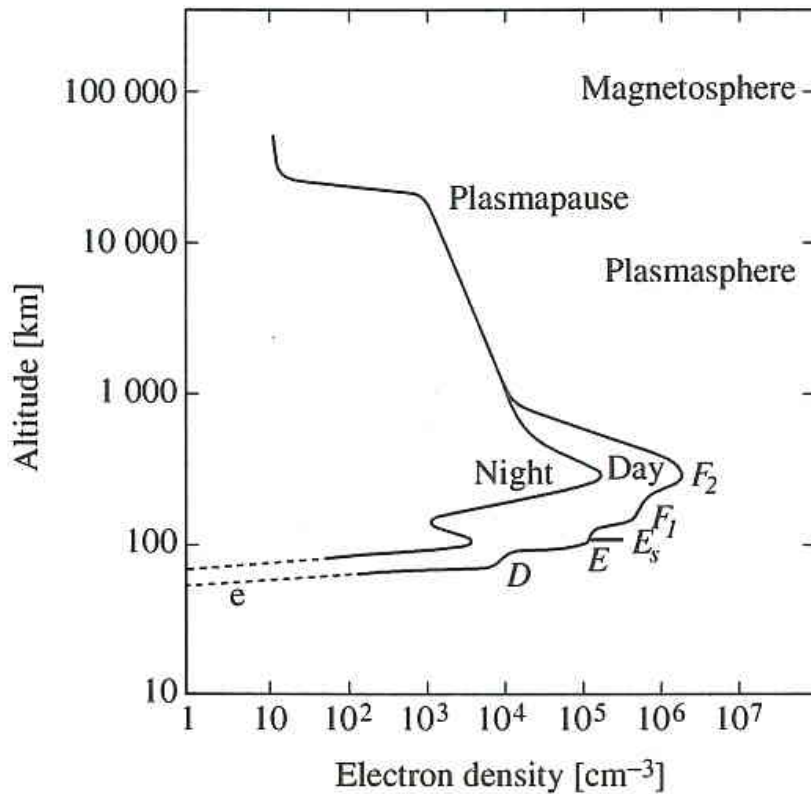


Figure 2.2: The regions of the ionosphere and electron density profile, [27].

2.4 The open-closed boundary

When the interplanetary magnetic field (IMF) from the sun, carried by the solar wind, connects to the Earth's magnetic field, this results in the open magnetic field line with one foot connected to the Earth and the other foot connected to the interplanetary magnetic field [16]. The boundary between the open field line and the closed field line is called the open-closed field line boundary (OCB) [15]. The ionospheric projection of the open-closed field line is also referred to as the polar cap boundary [6]. The open-closed field line boundary depends on the interplanetary magnetic field conditions, solar wind dynamic pressure and the tilt of the dipole axis [15].

Kabin et al. [15] used the steady-state magnetohydrodynamics (MHD) model to compare the change in open-closed field line boundary position with the change in the interplanetary magnetic field conditions, solar wind dynamic pressure and the tilt of the dipole axis. In this study it was found that when the B_z component of the interplanetary changes from northward to southward, this results in an increase in the polar cap area and there is a small expansion on the nightside of the polar cap [15].

The increased solar wind dynamic pressure leads to an increase in the area of open field lines. When the interplanetary magnetic field is directed southward, the polar cap area

is uniform at all magnetic local times. For a northward-directed interplanetary magnetic field the expansions of the polar cap is non-uniform when B_y is non-zero [15].

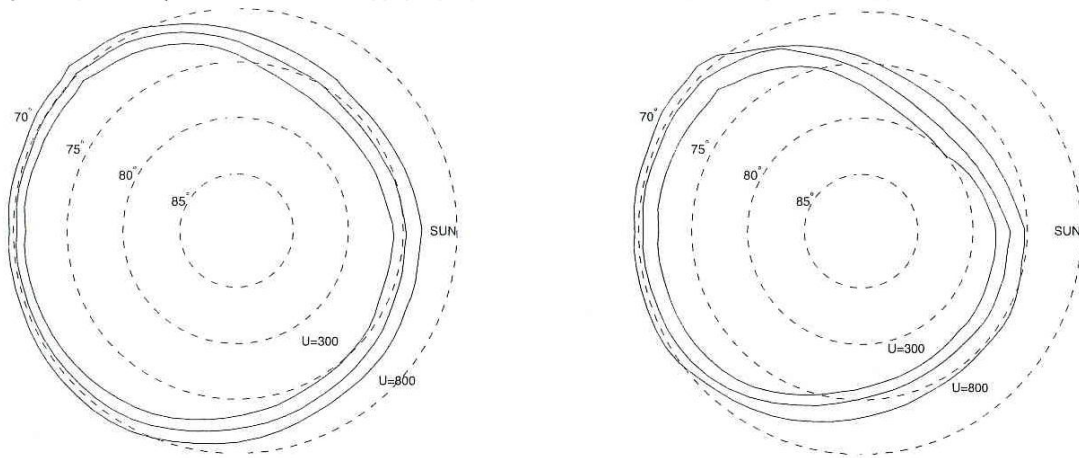


Figure 2.3: Open-closed field line boundary for $B_y = 5$ nT, $B_z = -5$ nT, $n = 5$ cm⁻³ and $U = 300, 500$ and 800 km/s (left) and open-closed field line boundary for $B_y = 5$ nT, $B_z = 0$ nT, $n = 5$ cm⁻³, and $U = 300, 500,$ and 800 km/s (right). The solar wind dynamic pressure is the same, [15].

The change in the B_x parameter of the interplanetary magnetic field has a small effect on the location of the open-closed field line boundary as compared to the B_y and B_z interplanetary magnetic field parameters [15]. The large change in the dipole tilt angle results in a latitude change of 1°-2° of the location of open-closed field line boundary. An example of change in open-closed field line boundary with change in velocity and the B_z interplanetary magnetic field parameter is shown in figure 2.3. For a more detailed discussion see [15].

2.5 The Magnetosphere and Ionosphere convection

The interplanetary magnetic field (IMF) carried by solar wind connects with the dayside Earth magnetic field. During the reconnection open field lines in the dayside are formed, and the solar wind particles enter the magnetosphere [20]. The open field lines are dragged by the solar wind towards the Earth's nightside. The strong anti-sunward flows are observed in the magnetopause and the flows decrease as they move inward as a result of the sunward flows in the plasmashet. The sunward flows are observed after reconnection of the open field line in the Earth's nightside and the interplanetary magnetic field electric field causes $\mathbf{E} \times \mathbf{B}$ plasma drift, called convection [28]. When the convection electric field is mapped down into the ionosphere through the magnetic field lines, two convection cells are observed in the north and south polar cap. The electric field perpendicular to the magnetic field changes the flow of ions and electrons and an increase in the ionospheric currents are observed. The flow of the ionosphere currents is sunward over the polar cap and is opposite to the plasma flow in this region. The electric field is from the dawn to

the dusk side in the high-latitudes and at lower latitudes it is from the dusk to dawn side. The convection in the ionosphere is supported by field-aligned currents and $\mathbf{J} \times \mathbf{F}$ force in the ionosphere [20]. The convection flow is from the dayside towards the nightside over the polar cap and sunward flows will be observed on the dawn and dusk side [27] and [20]. The convection pattern observed in the ionosphere strongly depends on the direction of the interplanetary parameter B_z carried by solar wind [28].

2.5.1 Dependencies of convection

The plasma of the high-latitudes ionosphere is kept in motion by the process that couples energy and momentum from the solar wind into the Earth's magnetosphere [28]. The plasma motion in the high-latitudes follows certain patterns, where it forms a two-cell configuration with the anti-sunward flow across the pole and the sunward flow in the dawn and the dusk side. The shape and the size of the convection cells depend on the direction of the interplanetary magnetic field carried by the solar wind and the seasons [28].

2.5.2 Interplanetary magnetic field dependencies

The convection in the ionosphere depends on the directions of the interplanetary magnetic field parameters B_y and B_z . The direction are given as follows: B_{z-} , B_{z+} , B_{y-} and B_{y+} .

B_{z+} and B_{z-} dependence

When the interplanetary magnetic field is directed northward (B_{z+}), the convection is weaker and this results in a decrease in cross polar cap potential [28]. The size of the convection cells decreases and the shape become crescent. There is more convection in the duskside than in the dawnside and the convection takes place at low-latitude [28]. This is shown in figure 2.4.

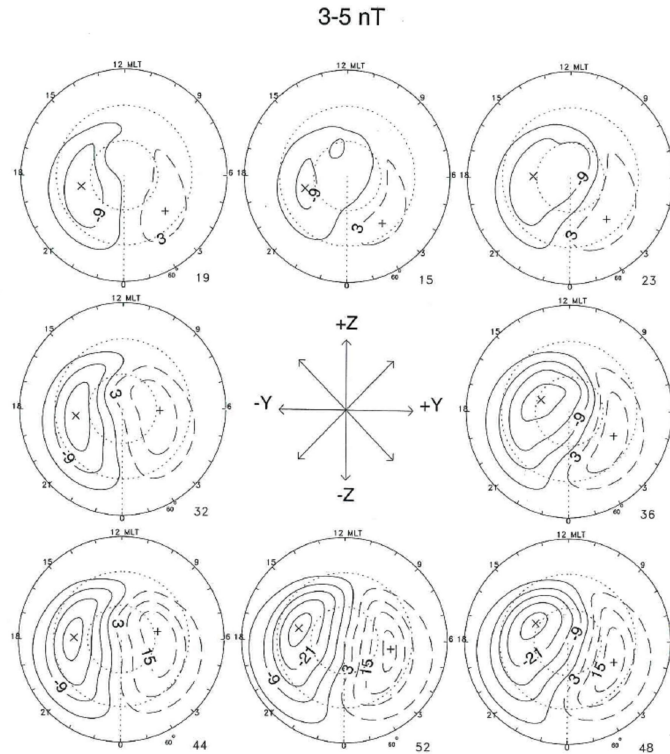


Figure 2.4: Statistical ionospheric convection patterns. The patterns depend on the IMF clock angle in the middle of the patterns, [28].

When the interplanetary magnetic field is directed southward (B_{z-}), the convection is stronger and this results in an increase in cross polar cap potential [28]. The dawn and dusk convection cells become rounder in shape and size increases. There is more convection in the duskside than in the dawnside and the convection takes place at high-latitude [28]. This is shown in figure 2.4.

B_{y+} and B_{y-} dependence

When the interplanetary magnetic field is directed towards the B_{y+} , this results in the dusk cells becoming more than the dawn cells. The dusk cell crosses the noon more to the dawnside. This results in the dusk cells becoming rounder and the dawn cells become crescent. The cross polar cap potential is consistently higher for B_{y+} than for B_{y-} [28] (See figure 2.4).

When the Interplanetary magnetic field is directed towards the B_{y-} , this results in an increase in the dusk cells and few cells in the dawnside. The convection cells in the duskside cross the noon to the dawnside and the cells become more crescent in the nightside. See figure 2.4 and for more discussion see [28].

2.5.3 Seasonal dependencies

A study using SuperDARN radars shows some changes in the convection due to seasonal changes. These changes are observed in the nightside and when B_z interplanetary magnetic field is dominated by the B_y parameter [28].

B_{y+} and Seasonal dependence

During B_{y+} in winter, the dawn cells are crescent in shape and the dusk cells are rounder in shape. The dusk cells cross the noon to the dawn side and the cross polar cap potential is higher than during the summer season [28]. The convection pattern during winter resembles the Ruohoniemi and Greenwald convection pattern model (RG05), (2005) and the polar cap potentials are basically equal [28] (See figure 2.5).

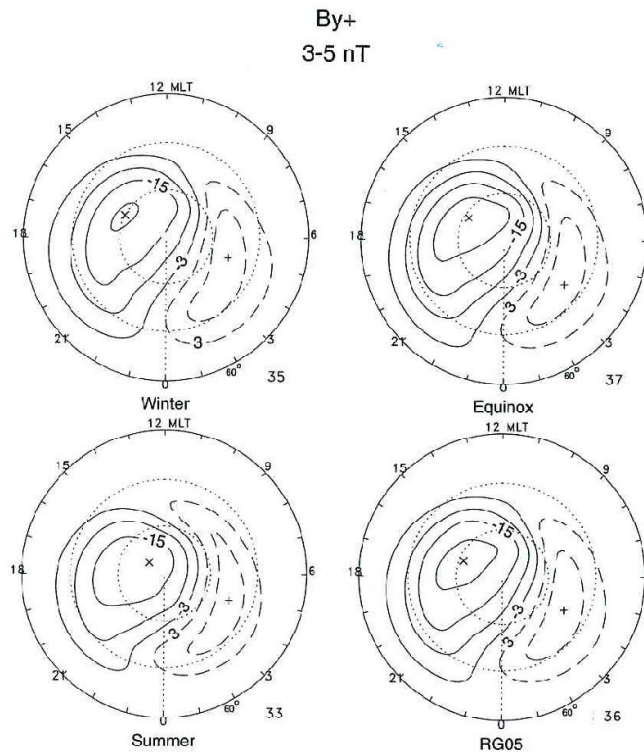


Figure 2.5: Statistical ionospheric convection patterns during the winter and summer seasons for predominantly IMF B_{y+} . The magnitude of the magnetic field was 3-5 nT, [28].

During B_{y+} in summer, the dawn cells are more crescent in shape and the dusk cells are rounder in shape. The dusk cells cross the noon to the dawn side and the cross polar cap potential is less than during the winter season [28]. See figure 2.5 and for more discussion see [28].

B_{y-} and Seasonal dependence

During B_{y-} in winter, the dusk cells cross the midnight meridian and there is more convection in the nightside. The cross polar cap potential decreases and is less than the potential of RG05 [28]. The dusk cells look more crescent in the nightside and the pattern does not look like the one of RG05 [28].

During B_{y-} in summer, the convection pattern resembles the one of the RG05 and there is more convection in the dawn cells than in the dusk cells [28]. The dusk cells look crescent in shape and the dawn cells are rounder in shape. The polar cap potential is higher than the polar cap potential in winter. See figure 2.6 and for more discussion see [28].

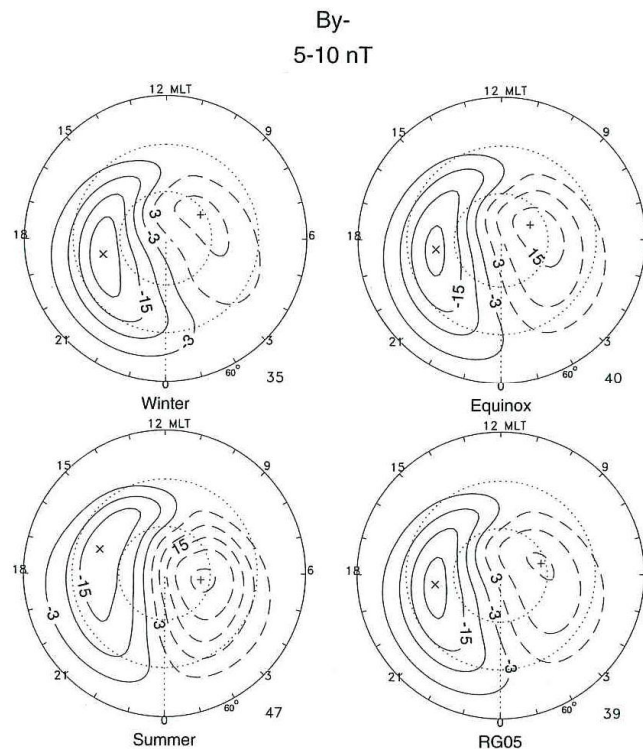


Figure 2.6: Statistical ionospheric convection patterns during the winter and summer seasons for predominantly IMF B_{y-} . The magnitude of the magnetic field was 5-10 nT, [28].

2.6 Magnetic field models

Geomagnetic field models are important tools for studying the shape and the structure of the Earth's magnetic field [10]. They help us to predict the field vector at all locations within the magnetosphere for all dipole tilt angles and the variations of the solar wind and magnetic activity [10]. The data-based magnetic field models are important for mapping the Earth's geomagnetic field. They also help to draw information from spacecraft data measured in the distant magnetic field and to understand the average geomagnetic field line configuration. Magnetic field models are also important for tracing the solar energetic particles in order to study the dynamics of the magnetosphere plasma [31].

2.7 The internal field model

The International Geomagnetic Field Reference (IGRF) model is a mathematical representation of the Earth's internal magnetic field and its secular variations [21]. The model represents the magnetic field generated by the internal sources and does not include the external sources. The spherical harmonic expansion is used to derive the model coefficients which are based on the data sets available [1]. The data used to derive the model coefficients are obtained from permanent magnetic field observatories, ships and spacecrafts [21]. The coefficients derived from the model are used to derive future model and this models are derived after five years [1].

2.7.1 Spherical harmonic representation of the main field

In 1839 Gauss showed that the potential of the geomagnetic field can be represented by a spherical harmonic series of the form [18],

$$V = \begin{cases} a \sum_{n=1}^{NMAX1} & \sum_{n=0}^n \left(\frac{a}{r}\right)^{n+1} [g_n^m \cos m\phi + h_n^m \sin m\phi] p_n^m(\cos\theta) + \\ a \sum_{n=1}^{NMAX2} & \sum_{n=0}^n \left(\frac{r}{a}\right)^n [q_n^m \cos m\phi + s_n^m \sin m\phi] p_n^m(\cos\theta) \end{cases} \quad (2.1)$$

where a is mean radius of the Earth, r , ϕ , θ are the standard spherical coordinates and $p_n^m(\cos\theta)$ are Schmidt quasi-normalized form of associated Legendre functions [18]. The least square procedure is used to derive the model coefficients g_n^m , h_n^m , q_n^m and s_n^m using field measurements. The internal and external coefficients vary with time and the n and m are referred to as the degree and the order of the equation [18]. The variation in the internal coefficients were modelled by expanding the coefficients of the Taylor series (see equation 2.2 below).

$$g_n^m = g_n^m(t_0) + \dot{g}_n^m(t_0) \times (t - t_0) + \ddot{g}_n^m(t_0) \times \frac{(t - t_0)^2}{2!} + \dots \quad (2.2)$$

The magnetic field is given by,

$$\mathbf{B} = -\nabla V = (B_r, B_\theta, B_\phi) \quad (2.3)$$

When equation 2.1 is derived, the values of $NMAX1$ and $NMAX2$ are limited by the data accuracy and the nature of the temporal variability of the external field. In equation 2.1 the term $\left(\frac{a}{r}\right)^{n+1}$ describes the internal sources and $\left(\frac{r}{a}\right)^n$ describes the external sources [18]. The first summation describes the field whose source is below the Earth's atmosphere (internal field) and the second summation describes the field whose source is outside the atmosphere (external field) [18]. If coefficients $|g_n^m|$, $|h_n^m| \gg |q_n^m|$, $|s_n^m|$, the part of the external field is ignored [18].

The data from magnetic observatories, spacecrafts, and survey ships and repeated measurements at selected sites with interval of one to six years were used to develop the magnetic field models. For further discussion see [18].

2.8 The external field model

The quantitative model of the external magnetospheric field is derived from various currents systems in the magnetosphere [10]. The current systems which are used to derive the models are: magnetopause current, ring current and tail current. This models includes the spherical harmonic expansion for good representation of changes in the magnetic field [10]. The model uses large data from the spacecrafts. The least square method is used to fit the data in order to obtain the model coefficients [10] and [25]. The magnetic activity data (K_p and Dst), solar wind dynamic pressure and interplanetary magnetic field parameters are used in these models [31].

2.8.1 The Tsyganenko T96 field model

During recent years Tsyganenko developed magnetic models T82, T87 and T89 using empirical data. These models combine the currents models with the polynomial technique and utilises a large data set [10]. The T82, T87 and T89 magnetic field models have three problems [31]. (i) The models cannot represent the stable magnetopause, (ii) they use the K_p index (magnetic activity index) is available at interval of 3 hours and indicates the degree of disturbance which is already in the Earth and the surrounding space [31] and (iii) the shape of the magnetosphere at the tail deviates from the expected location [31].

Due to the problems with the T82, T87 and T89, the Tsyganenko T96 model was developed in such away as to address the problems encountered by the previous three Tsyganenko field models. The T96 field model has the following new features:

- A realistic shape and size of the magnetopause,
- Fully controlled shielding of the magnetic field produced by all the magnetospheric currents,
- A new flexible representation of tail and ring currents, and
- A new criterion for fitting model field to spacecraft data, providing improved accuracy for field line mapping.

For a detailed discussion of the new features of the T96 magnetic field model, see [31] and [32]. The external field is given by:

$$\mathbf{B}_E = \mathbf{B}_{MP} + \mathbf{B}_{RC} + \mathbf{B}_T + \mathbf{B}_{R1} + \mathbf{B}_{R2} + \mathbf{B}_{INT} \quad (2.4)$$

where B_{MP} is the magnetopause current field, B_{RC} is the ring current field, B_T is the tail current field, B_{R1} and B_{R2} are region 1 and 2 Birkeland currents and B_{INT} is the interaction between the interplanetary magnetic field and magnetosphere field [31]. The model depends on the interplanetary magnetic field parameters B_y and B_z , solar wind dynamic pressure and the magnetic activity (Dst index). Figure 2.7 shows the projection of the model field lines when the interplanetary magnetic field is strongly northward.

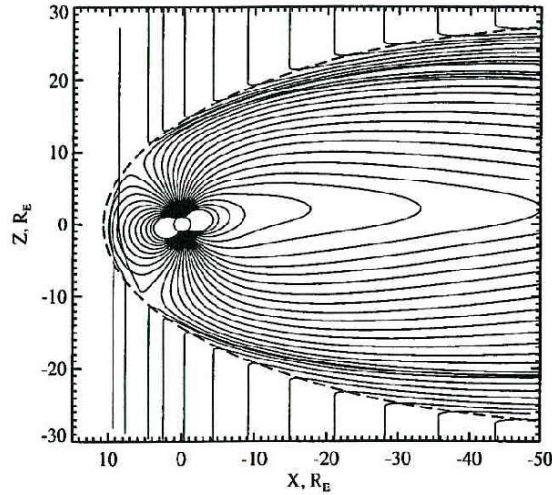


Figure 2.7: The noon-midnight projection of geomagnetic field lines during strong northward directed IMF. The solar wind dynamic pressure (P_{dyn}) = 2.5 nPa, IMF B_y = 4.0 nT and B_z = +10.7 nT, [32].

2.8.2 Field line trace

If we have a point in space defined in terms of the radius, and the latitude and longitude coordinates system, the Tsyganenko field model can be used to trace the footprint of the point in the ionosphere. The model allows us to trace field lines in two different directions (the two directions are parallel or anti-parallel to the field line). The trace method also helps us to identify open and closed field lines.

In figure 2.8, plot (parallel) shows the field line trace from point X in space parallel to the magnetic field into the surface of the Earth and plot (antiparallel) shows the field line trace from point X space anti-parallel to the magnetic field to surface of the Earth.

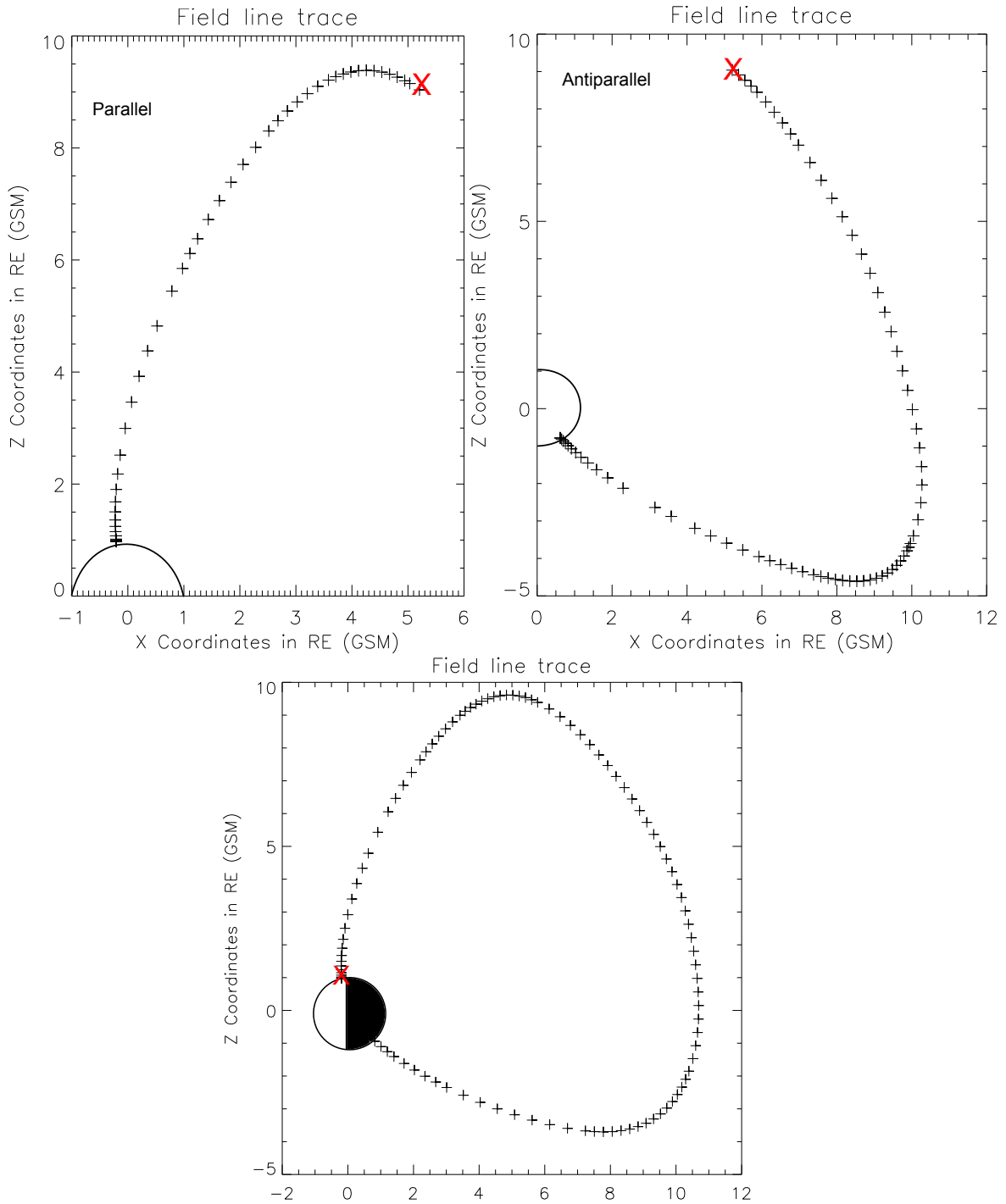


Figure 2.8: Field line trace from space to northern hemisphere (left) and field line trace from spacecraft to southern hemisphere (right). The field lines were traced with the Tsyganenko T96 field model.

The plots started at $x = 5.2 R_E$, $y = 5.1 R_E$ and $z = 9.7 R_E$ and ends in the ionosphere. In plot (bottom), the field line is traced from point X in the northern hemisphere ionosphere to the southern hemisphere ionosphere. The magnetic field coordinates used in bottom plot were calculated using the Tsyganenko T96 field model. We can conclude that the spacecraft was crossing a closed field line, since both feet of the field line are connected to

the Earth.

2.8.3 Footprint plots

If we have a spacecraft crossing the field of view of SuperDARN radar, the spacecraft magnetic footprint can be traced using the Tsyganenko model to map its location in the radar field of view. If the field line is closed, the spacecraft's magnetic footprint can be mapped in both the northern and southern hemisphere. If the field line is open it can also be identified using the Tsyganenko field model. Only one end of the field will be in the ionosphere and the other will be in space.

In figure 2.9 the green stars represent the spacecraft's magnetic footprint, red numbers represent universal time (UT) in hour intervals and the triangles represent the field of view of SuperDARN radars in the southern hemisphere.

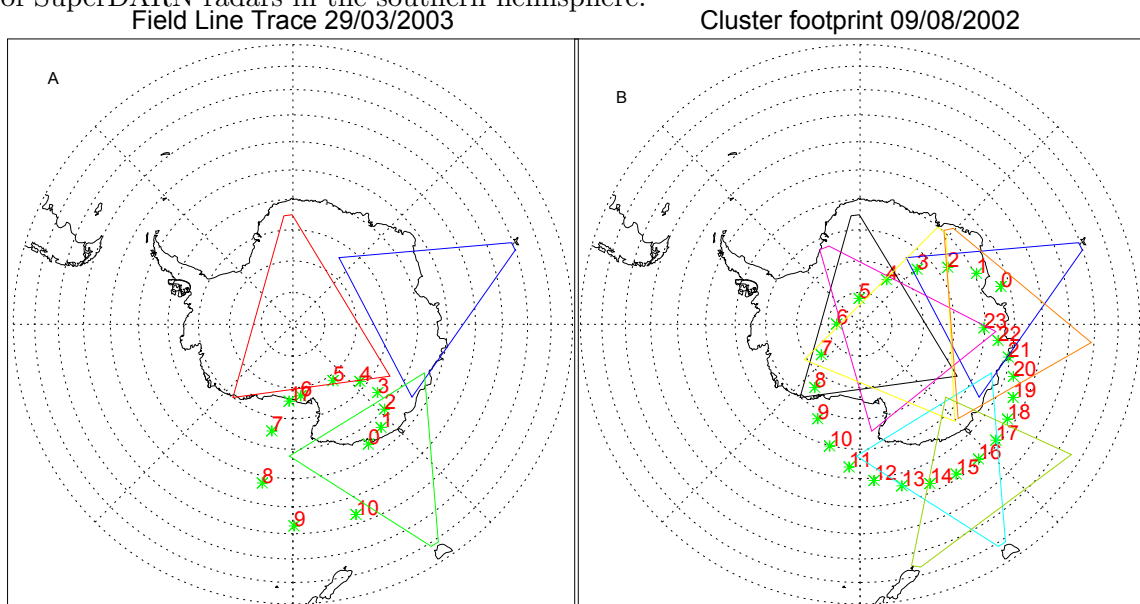


Figure 2.9: Spacecraft's magnetic footprint mapped using the Tsyganenko T96 field model. The green stars represent footprint, red numbers represent universal time (UT) in hours and the triangles represent the field of view of SuperDARN radar in the southern hemisphere.

Looking at plot A, we notice that the footprint starts at midnight (00 UT) and continues until 10 UT and another footprint starts at 17 UT. This tells us that between 10 UT and 17 UT the spacecraft was moving across the open field lines and after 17 UT the spacecraft was moving across the open field lines. Looking at plot B, we see that throughout the day the spacecraft was moving across closed field lines.

2.9 Conclusion

This chapter described the regions of the magnetosphere and ionosphere, and the magnetic field models. Since the processes observed in the high-latitude are influenced by the solar

wind, the properties of the solar wind were discussed in section 2.1. Section 2.4 dealt with open-closed field line boundary and the factors that affect it. Section 2.5 dealt with convection in the high-latitudes and the factors that affect it.

In this study the observations in the magnetosphere by the Cluster spacecraft will be compared with the observation made by SuperDARN radar in the high-latitude ionosphere. The field models will be used to map the magnetic footprint of the spacecraft into the ionosphere. In section 2.6 the internal field and external field models were discussed (see section 2.7 and section 2.8). The Tsyganenko external field model and model input parameters to be used in this study were discussed in section 2.8.1. The field line trace plots generated using the Tsyganenko field model were shown and discussed in subsection 2.8.2. The Cluster magnetic footprint plots which were generated using the Tsyganenko field model were discussed in subsection 2.8.3. The figures are useful if we want to see whether the spacecraft was crossing open or closed field lines. If the footprint of the spacecraft during a certain period cannot be mapped to the ionosphere, it shows that during that time interval the spacecraft was crossing an open field line (see figure 2.9 A). The data from the different regions of the magnetosphere and ionosphere can be obtained from Cluster and SuperDARN radar. For information on Cluster and SuperDARN see chapter 3.

Chapter 3

Instruments and data format

This chapter discusses the instruments used in this study, namely their location, operation and data format. Three instruments were used: ACE, the Cluster satellite and SuperDARN radar. ACE and Cluster are space-based instruments operating in different regions in space. The SuperDARN radars are ground-based instruments located at the north and south poles. The electric field measured by Cluster will be compared with the line of sight velocity observed by SuperDARN radar. The ACE satellite monitors the changes in the solar wind and interplanetary magnetic field before they reach the Earth.

3.1 Super Dual Auroral Radar Network (SuperDARN)

High frequency (HF) radars are important tools for studying the behaviour of the Earth's ionosphere [11]. Super Dual Auroral Radar Network (SuperDARN) is a global network of HF coherent-scatter radars capable of observing small-scale irregularities in the E and F-regions of the ionosphere [11]. The SuperDARN radars are located in the northern and southern hemispheres (see figure 3.1). There are 11 SuperDARN radars in the northern hemisphere and 7 radars operating in the southern hemisphere. The radar field of view is shown in figure 3.1.

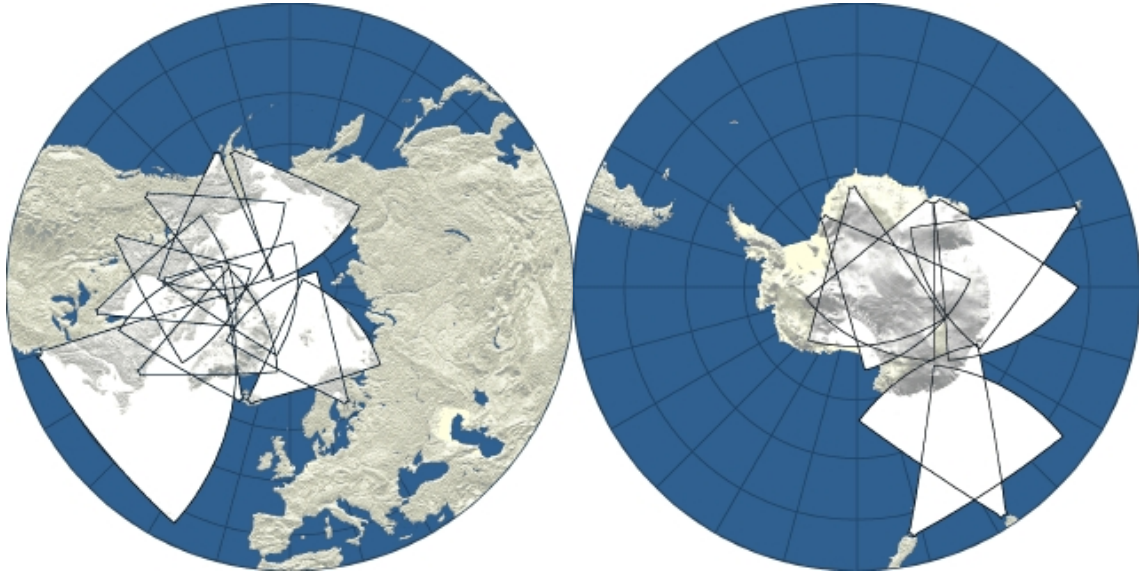


Figure 3.1: SuperDARN radars in the northern hemisphere (left) and SuperDARN radars in the southern hemisphere (right).

The radars operate at a high frequency of 8 - 20 MHz and in pairs with an overlapping field of view [33]. When the data from two radars with an overlapping field of view is merged, the drift velocity vector can be determined [33]. The data from all the radars operating in the same hemisphere are combined with solar wind data to produce a map of high-latitude ionospheric convection [7].

The typical SuperDARN radar consists of an array of 16 broadband log-periodic antennas capable of transmitting and receiving HF signals [33] (see figure 3.2).



Figure 3.2: SuperDARN antenna array at SANAE, Antarctica.

The beam formed by the radar can be directed into 16 directions making a total of 16

beams, with an angular separation of 3.3° between the beams [33]. The beam width depends on the transmitting frequency. If the radar transmits at 20 MHz, the beam angle is 2.5° and if the radar transmits at 8 MHz, the beam angle is 6° [33].

The radar beam is divided into 75 ranges and each range is 45 km [33]. A SuperDARN radar have typical scan of 120s through all range gates and beams, and this gives the radar a large spatial region of about $2000 \times 2000 \text{ km}^2$ to measure the properties of the irregularities [33]. When the signal is transmitted from the radar into the ionosphere, backscatter can only be achieved if the transmitted signal is orthogonal to the magnetic field line [11] (see figure 3.3).

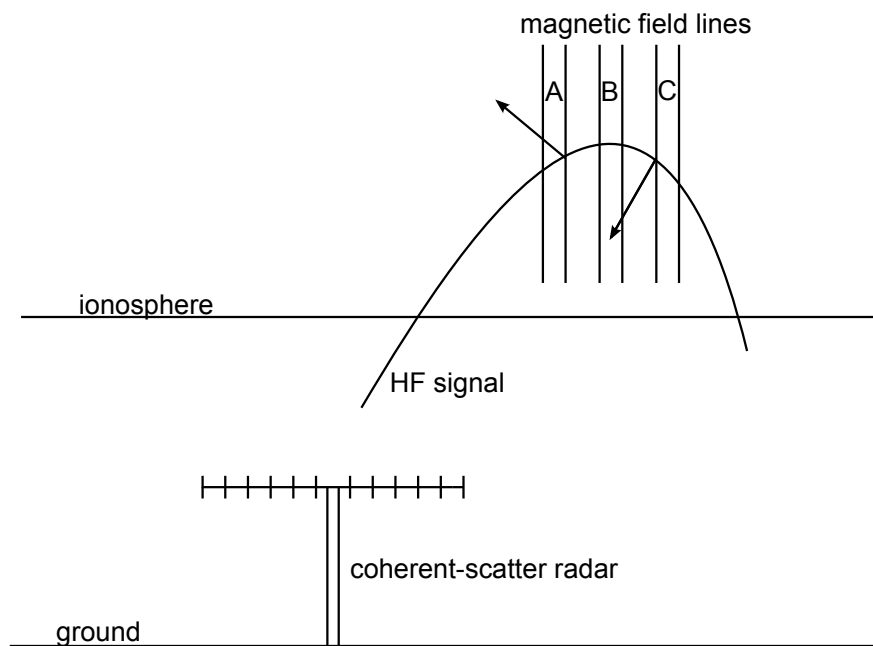


Figure 3.3: The HF signal transmitted by the radar to the ionosphere, [33].

When the signal reaches the field line at point A and C it will be refracted into space because at those positions the signal is not perpendicular to the magnetic field (see figure 3.3). Backscatter to the radar site will happen at point B, because the signal is orthogonal to the magnetic field [11], [33]. The returning signal is sampled and multi-lag autocorrelation is produced as a function of range [7]. The backscatter power, line of sight doppler velocity and spectral width plots of each beam are produced [7]. See an example of a time plot in figure 3.4.

3.2 The Cluster satellite

The Cluster mission was proposed by the European Space Agency (ESA) in 1982 and it was launched during the summer of 2000 [9], [5]. The mission consists of four identical spacecrafts and each spacecraft having 11 scientific instruments. The Cluster has a polar orbit with a perigee of $4 R_E$ and an apogee of $19.6 R_E$ [9]. The spacecrafts are cylindrical in shape with a diameter of 2.9 m, height of 1.3 m and total mass of 1200 kg. The four spacecrafts form a tetrahedron configuration during the orbit and the separation distance between them varies from 200 km to 1800 km [9].

The main objective of the mission is to study three dimensional small-scale plasma structure in space and time in the plasma regions. The plasma regions of interest for the Cluster mission are as follows [9]:

- Solar wind and bow shock
- Magnetopause
- Polar cusps
- Magnetotail
- Auroral zone

For more on how the Cluster mission answers scientific questions, see [9].

The Cluster mission has an orbital period of 57 hours. In the initial stage, the spacecrafts have a dawn to dusk orbit with the apogee on the duskside [9]. After 3 months the apogee is at local noon and the position of the apogee changes every 3 months until it reaches the initial position after a year [9] (see figure 3.5).

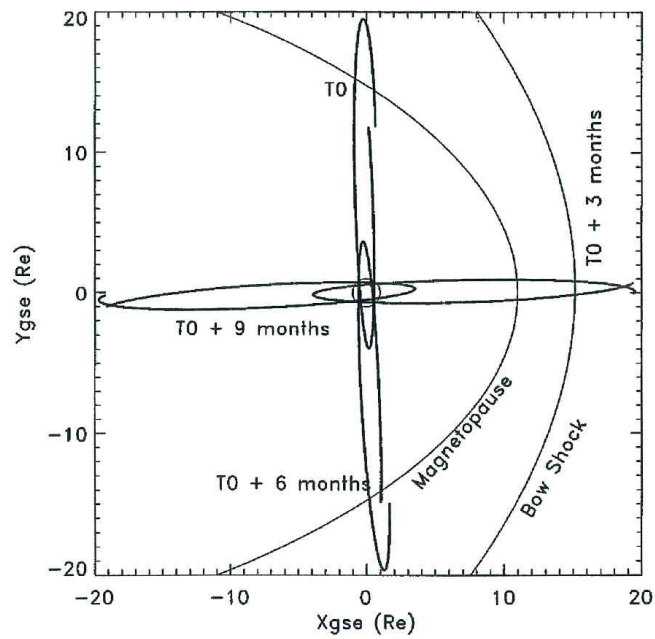


Figure 3.5: Cluster spacecraft orbit during the first year of the mission, [9].

When the apogee is at local noon or local midnight, the spacecraft has the opportunity to observe the auroral zones, cusps, magnetopause, bow shock and solar wind. All these observations are made in both the northern and southern hemispheres [9] (see figure 3.6).

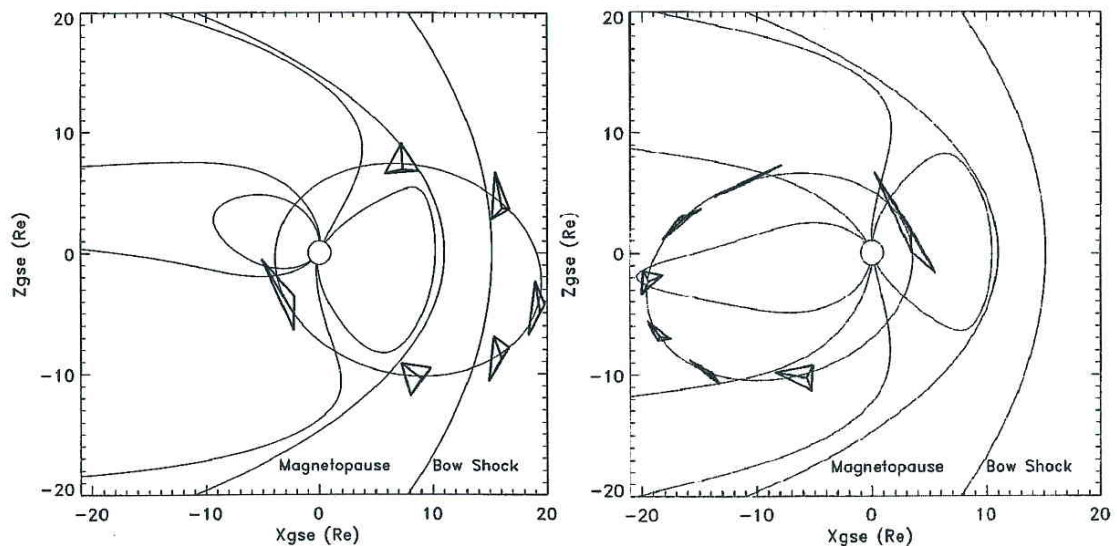


Figure 3.6: Spacecraft configuration when the apogee is at local noon, local midnight and magnetotail, [9].

The separation between the spacecrafts when they cross the region of interest is described in [9]. When the apogee is at the tail, the spacecraft is able to observe the mid-latitude

cusps, polar cap, tail lobes and plasmashet (see figure 3.6). During the second year of the mission, the separation need was set to be between 200 km and 2000 km [9].

3.2.1 Electric Field and Wave (EFW) instrument

In this thesis the data from the Electric Field and Wave (EFW) instrument on board the Cluster spacecrafts was used. The Electric Field and Wave instrument is one of the 11 instruments and is located at the ends of the 50 m long booms. It is capable of measuring small, intermediate and large-scale plasma structure in plasma regions [14]. The EFW instrument is capable of measuring wave phenomena with temporal resolution of 110 μ s and taking full waveforms up to 180 Hz. One of the objectives is to study intermediate magnetohydrodynamic turbulence in the solar wind, magnetosheath and cusps [14]. The EFW data is also used to study spatial and temporal variation in the auroral zones and waves associated with quasi-parallel shock, flux transfer events and impulsive penetration plasma in the magnetosphere associated with reconnection [14]. Comparison of the data from the EFW instrument and SuperDARN will lead to a better understanding of the ionospheric convection. For more details on the electric field and wave experiment, see [14].

3.3 The Advanced Composition Explorer (ACE) satellite

The Advanced Composition Explorer (ACE) is a mission of the National Aeronautics and Space Administration (NASA) to study solar wind - magnetosphere - ionosphere coupling [26]. The spacecraft was launched on 25 August 1997 by a Delta II rocket [29]. The spacecraft is located 240 R_E sunward of the Earth and contains of 9 scientific instruments [29]. The plasma and the interplanetary magnetic field carried by the solar wind have an influence on the processes taking place in the magnetosphere and ionosphere [16]. In this study the solar wind and the interplanetary magnetic field data will be used. The ACE data is available on the URL: http://cdaweb.gsfc.nasa.gov/cdaweb/istp_public. The plots of the interplanetary magnetic and solar wind velocity data measured by the ACE spacecraft on 03 August 2004 are in figures 3.7 and 3.8.

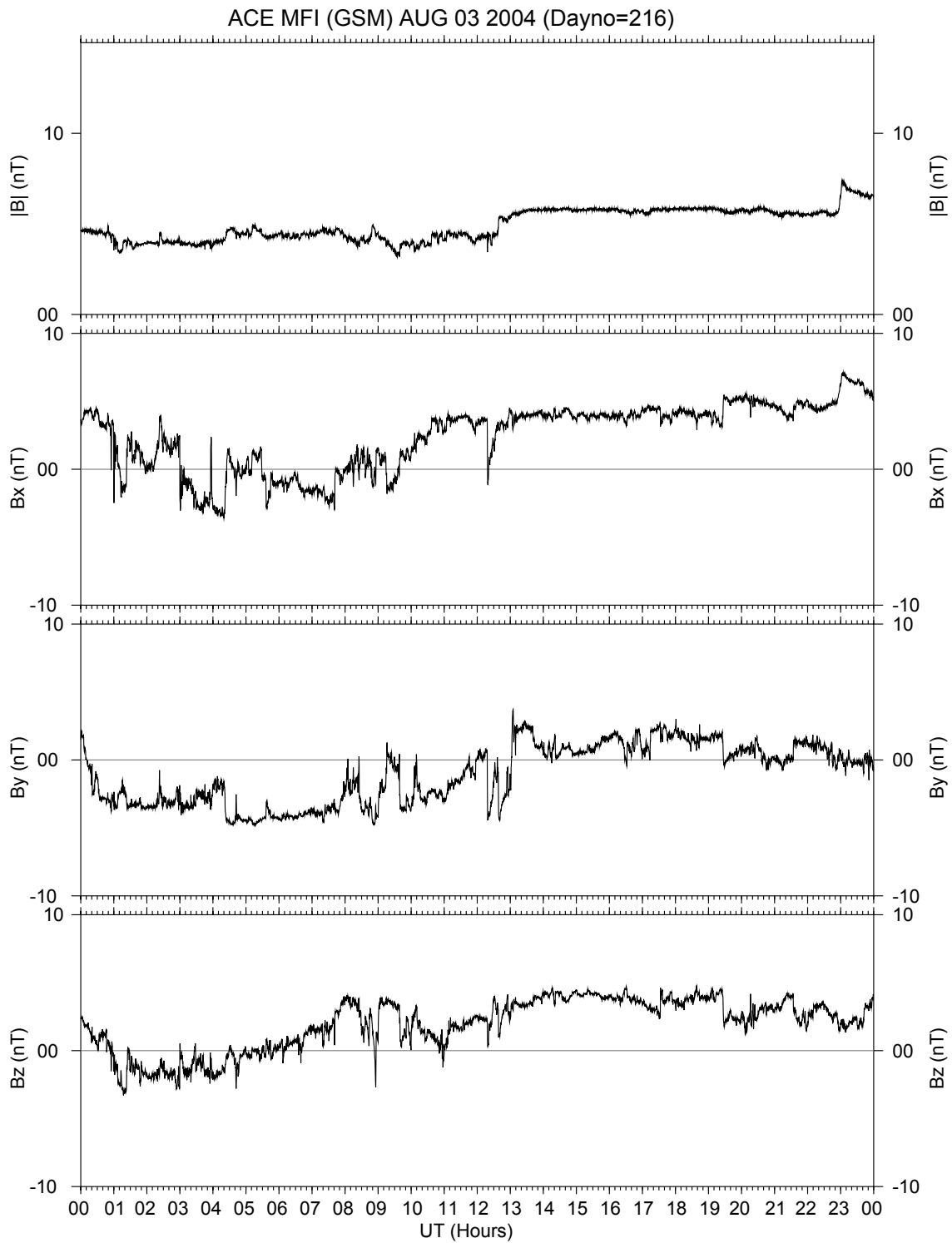


Figure 3.7: Interplanetary magnetic field measured by ACE spacecraft in Geocentric Solar Magnetic coordinates on 03-08-2004 for the time interval 00 to 00 UT. The plot was produce using SuperDARN data analysis software.

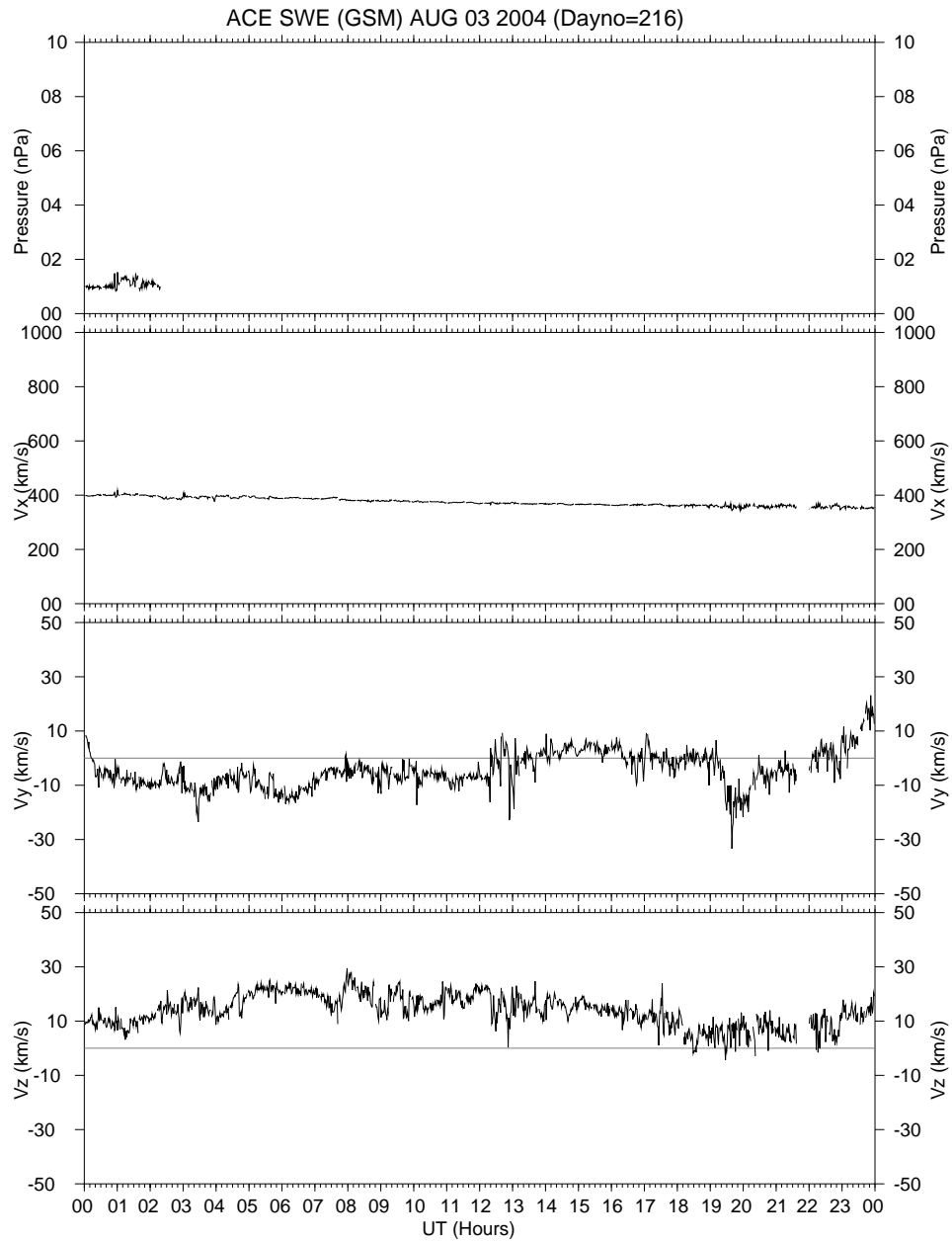


Figure 3.8: Solar wind velocity measured by ACE spacecraft in Geocentric Solar Magnetic coordinates on 03-08-2004 for the time interval 00 to 00 UT. The plot was produced using SuperDARN data analysis software.

In figure 3.7 the top panel shows the total field, followed by the B_x , B_y and B_z interplanetary magnetic field parameters. In figure 3.8, the top panel show the solar wind dynamic pressure measured by the ACE spacecraft, followed by the solar wind velocity components (V_x , V_y and V_z) in Geocentric Solar Magnetic (GSM) coordinates.

3.4 Conclusion

The SuperDARN radar and its operation was discussed in section 3.1. The time series plot, generated from SuperDARN radar data, in figure 3.4 and shows the backscatter power, line of sight doppler velocity and spectral width. The Cluster spacecraft, one of the instruments used in this study, observes different regions of the magnetosphere, as given in section 3.2. The orbit of the spacecraft and the time of year when the spacecraft crosses some regions of interest is given in figures 3.5 and 3.6. The electric field data measured by the Electric Field and Wave form (EFW) instrument on board of the Cluster spacecraft is used in this study. A brief discussion of the electric field and wave form instrument was given in subsection 3.2.1. The ACE satellite data is also important in this study. The interplanetary magnetic field parameters are used in the Tsyganenko field model as one of the input parameters. The solar wind dynamic pressure is for mapping spacecraft footprint into the ionosphere. The IMF parameters B_y and B_z are used for generating convection by means of the SuperDARN data analysis software. A brief discussion of the ACE satellite is given in section 3.3 and some ACE data plots are given in figures 3.7 and 3.8.

Chapter 4

Survey of Cluster and SuperDARN radar successes

This chapter looks at successes using data from Cluster, SuperDARN and other satellites and ground-based instruments. Since the commission of SuperDARN radar in 1983, it is now easier to understand the flow of high-latitude irregularities in the polar ionosphere. Since SuperDARN radars have overlapping fields of view, two dimensional flow of the irregularities in ionosphere can be observed. The instrument location also plays an important role in the observation of changes in the polar ionosphere, since the solar wind particles access the Earth's atmosphere at the poles due to open field lines at the polar cap. The observations made by SuperDARN were confirmed by ground-based instruments and low orbit satellites. The commission of the Cluster mission in 2000 increased understanding of the observations made by SuperDARN, low orbit satellites and ground-based instruments. Since Cluster spacecrafts make the measurements in the magnetospheric regions. For more information on the regions covered by Cluster, see chapter 3. The 11 instruments on board each of the four spacecrafts make it possible for the space physicist to study different regions of geospace. The orientation of the four spacecrafts make it possible to confirm the observations made by the other spacecrafts.

4.1 Successes using SuperDARN radar and Cluster data

In this section the results obtained using data from SuperDARN radar and other instruments are discussed, followed by results obtained using Cluster and SuperDARN radar data. The aim is to show how research can be promoted using these instruments which are in different locations. This section also gives an idea of research that has been done and how one can combine the different instruments to study changes in the space environment.

4.1.1 Successes using SuperDARN radar data

- Taylor et al. [30] investigated the response of ionospheric convection when the interplanetary magnetic field was initially southward and it turned northward. In this investigation two ground-based instrument, including SuperDARN radar, and one space-based instrument (DMSP) were used. Due to the change in the interplanetary magnetic field, a change in convection cells from twin to multiple and reverse convection flow was observed [30].
- Yeoman et al. [36] used a combination of the data from SuperDARN radar and EISCAT heaters at Tromsø to investigate ultra low frequency processes. More than three different waves were observed and their information was combined in order to divide them according to their scales [36].
- McWilliams et al. [24] observed flux transfer (FTE's) events using the data from the Geotail, DMSP F11, IMP-8 and SuperDARN radar for a short period (4 hours) and during this period the interplanetary magnetic field was directed northward. Flux transfer events were observed by Geotail and these were confirmed by the dawn sector SuperDARN radar observations and DMSP F11 observations in the southern hemisphere [24].
- Koustov et al. [17] investigated the relationship between SuperDARN radar E-region echoes and $\mathbf{E} \times \mathbf{B}$ plasma drift in the F-region measured by DMSP satellites. The results from the investigation show that the ratio of HF velocity to DMSP is ~ 0.35 in a DMSP range of 0 - 1700 m/s [?].
- Grocott et al. [13] used SuperDARN radar data to study the signatures of tail reconnection in both northern and southern hemispheres when the interplanetary magnetic field was directed northward and the B_y component changing from negative to positive. During B_{y-} the convection flow in the northern hemisphere was opposite direction compared to the convection in the southern hemisphere, and when B_y changed from negative to positive a reverse convection was observed in both hemispheres [13].
- Grocott et al. [12] used SuperDARN radar and Cluster data to investigate flux transport during northward directed and dominating B_y interplanetary magnetic field. For the investigation two events were used and it was found that flux flow observed by Cluster was consistent with convection flow observed by SuperDARN radar [12].
- Marcucci et al. [23] used the SuperDARN radar data to study the ionospheric convection in the northern hemisphere for a short period when the interplanetary magnetic field was directed northward and the B_y component changing from negative to positive. Cluster satellite data reveals a tailward magnetic reconnection site and

the data from SuperDARN, IMAGE FUV and DMSP confirm this observation by Cluster [23].

4.1.2 Successes using Cluster data

- Lockwood et al. [19] observed ionospheric flow enhancement when the interplanetary magnetic field was directed southward, the Tsyganenko T96 field model was used to map the magnetic footprint of Cluster into the ionosphere and the footprint was found within the field of view of EISCAT Svalbard SuperDARN radar. For a short period (8:00 - 9:30 UT), the ionospheric flow enhancement was observed by both Cluster and SuperDARN radar.
- Wild et al. [34] observed magnetospheric flux transfer events using Cluster when the interplanetary magnetic field was directed southward. The magnetic footprint of Cluster was mapped into the ionosphere using T96 magnetic field model and it was found within the field of view of CUTLASS SuperDARN radar and also in the field-aligned beam of the EISCAT Svalbard radar system [34]. The pulse ionospheric flow was observed by the radar which was a confirmation of the coupling of energy and momentum into the magnetosphere-ionosphere system [34].
- Marchaudon et al. [22] investigated the correlation between Cluster and SuperDARN radar data when the interplanetary magnetic field was initially directed northward and duskward and turned southward and dawnward for a short period of time. The investigation found a one-to-one correlation between SuperDARN radar and Cluster [22].
- Wild et al. [35] used ground-based and space-based instruments were used to investigate dayside magnetic reconnection when the interplanetary magnetic field was directed duskward. A newly reconnected flux tube was observed by Cluster, Double star and SuperDARN radar [35].
- Eriksson et al. [8] used Cluster satellites data to study ultra low frequency (ULF) wave events during quiet magnetic conditions. The phase shift and the azimuthal separation between the spacecrafts was used to find the azimuthal wave number for the events [8]. Large azimuthal waves in poloidal mode were found and they were consistent with the large wave number [8].

4.2 Conclusion

Results obtained using data from Cluster, SuperDARN and other instruments were discussed. In the work done by [34] and [35], the Cluster and ACE FGM magnetometer data were used to observe flux transfer events (FTE). The enhancement observed by both

Cluster and ACE was compared to line of sight velocity observed by radar. Marchaudon et al. [22] used the CIS instrument on board of Cluster spacecraft to compare the ion velocity observed by Cluster with the line of sight velocity observed by SuperDARN radar. A one-to-one correlation and time delay was observed [22]. In the work done by Eriksson et al. [8] the data from FGM and EFW instruments was used to study the poloidal ULF waves. Looking at work which has been done using different instruments on board Cluster, low orbit satellites and ground-based instruments, one can see that multiple observations can help to answer questions scientists have for long time. This comparison is made possible by means of a magnetic field model which maps the magnetospheric events into the ionosphere.

Chapter 5

Data analysis techniques

This chapter describes the procedures used to generate time series, field of view and convection maps using the SuperDARN data analysis software. After each procedure, an example of a generated plot is shown and briefly discussed. A description of each tool used in the procedure and its purpose. The website where the software can be found is provided.

5.1 SuperDARN data analysis software

The SuperDARN toolkit is a data analysis software package developed by Rob Barnes for the SuperDARN radar data users. The software consists of different tools capable of analysing and generating plots, such as interplanetary magnetic field plots, vector and convection map plots. The software is available on the SuperDARN website [3]. For a discussion of the software, see [3] and [4].

5.1.1 Time series plots

The SuperDARN data is stored in different formats, namely fit, fitacf and data files and each data file contains 2 hours worth of data. This means that for one day you have 12 data sets which differ by 2 hours. In this study the fit files were used to generate time series plot. Four steps are needed in order to generate time series plot:

- Step one: concatenate the data from the fit files of each radar to make a data set of 24 hours or one day using tool `cat_fit` [4].
- Step two: convert the 24 hours fit file generated in step one into fitacf using the tool `fittofitacf` [4].

The new fitacf file must also have a radar code for identification.

- Step three: compress the fitacf to form cfit file using the tool `make_cfit` [4]. The cfit file is used to generate a time series plot.

When the cfit file has been generated the minimum power has to be set and the radar code must also be included in the file name.

- Step four: use the `time_plot` tool to plot the time series plot [4].

The `time_plot` tool allows one to zoom into the plot. This is achieved by setting the range and the time of interest. Since the radar is divided into 16 beams, one can also use this tool to choose the beam of interest. The time series plot is divided into three panels and the tool allows the user to plot all panels or choose one of the three panels for analysis. This plots time versus range, see figure 5.1. A detail description is found in appendix A.1.1.

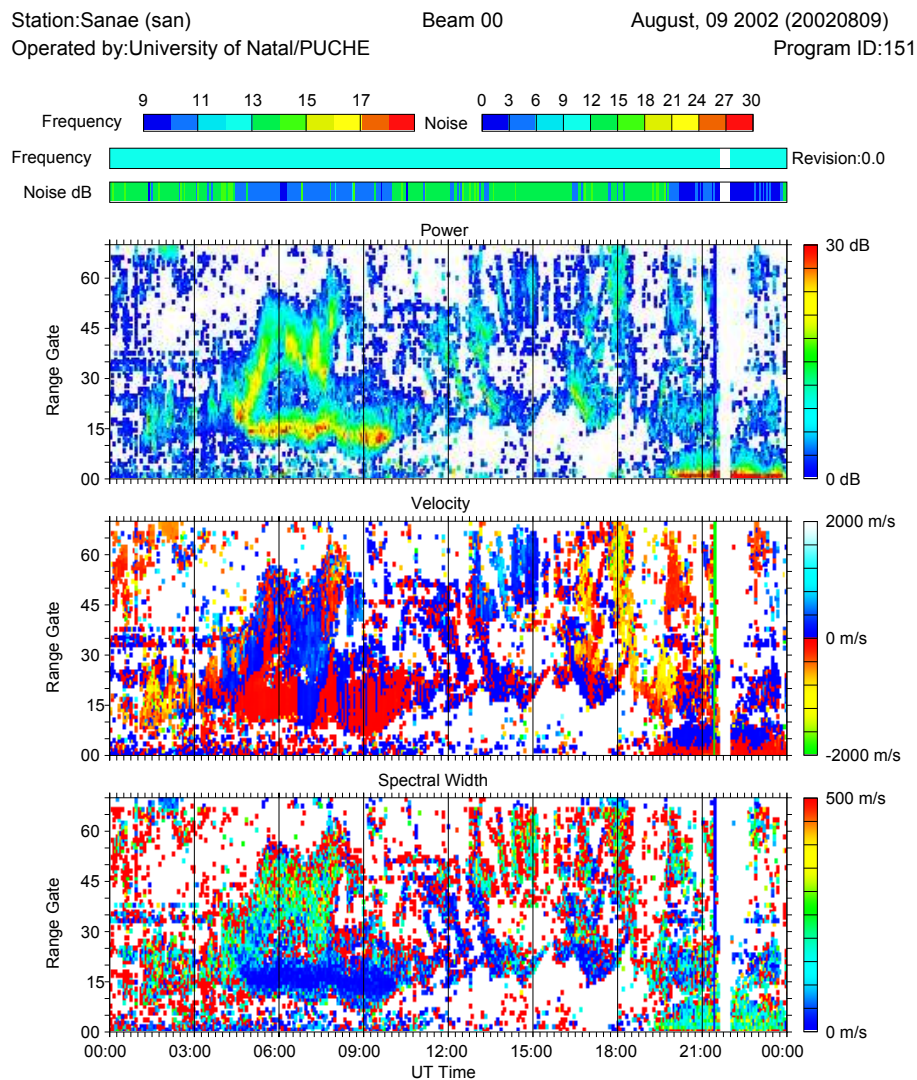


Figure 5.1: Time series plot: backscatter power (top panel), the line of sight doppler velocity (middle panel) and spectral width (bottom panel). The plots were produced using SuperDARN data analysis software.

The plot is divided into three panels, the backscatter power (top), line of sight doppler velocity (middle) and spectral width (bottom). The backscatter power is plotted in terms of signal to noise in decibel (dB) units, the velocity in meter per second (m/s) and the spectral width in meter per sec (m/s). In the middle panel (velocity), the red colour shows that the irregularities are moving away from the radar and the blue shows that the irregularities are moving towards the radar.

5.1.2 Field of view plots

The data format which was used to generate time series plots in section 5.1.1 is the same as the one for generating field of view plots. The data processing procedure for field of view plots is similar to the one followed for time series plots. The difference between the two procedures is the tool that is used in step four. In the time series plot the tool `time_plot` is used whereas in the field of view plot the tool `field_plot` is used [4]. For a detail description see appendix A.1.2.

The `field_plot` tool generates the plot of the backscatter observed by the radar and when using this tool one has to choose whether to generate backscatter power, line of sight doppler velocity or spectral width (see figure 5.2).

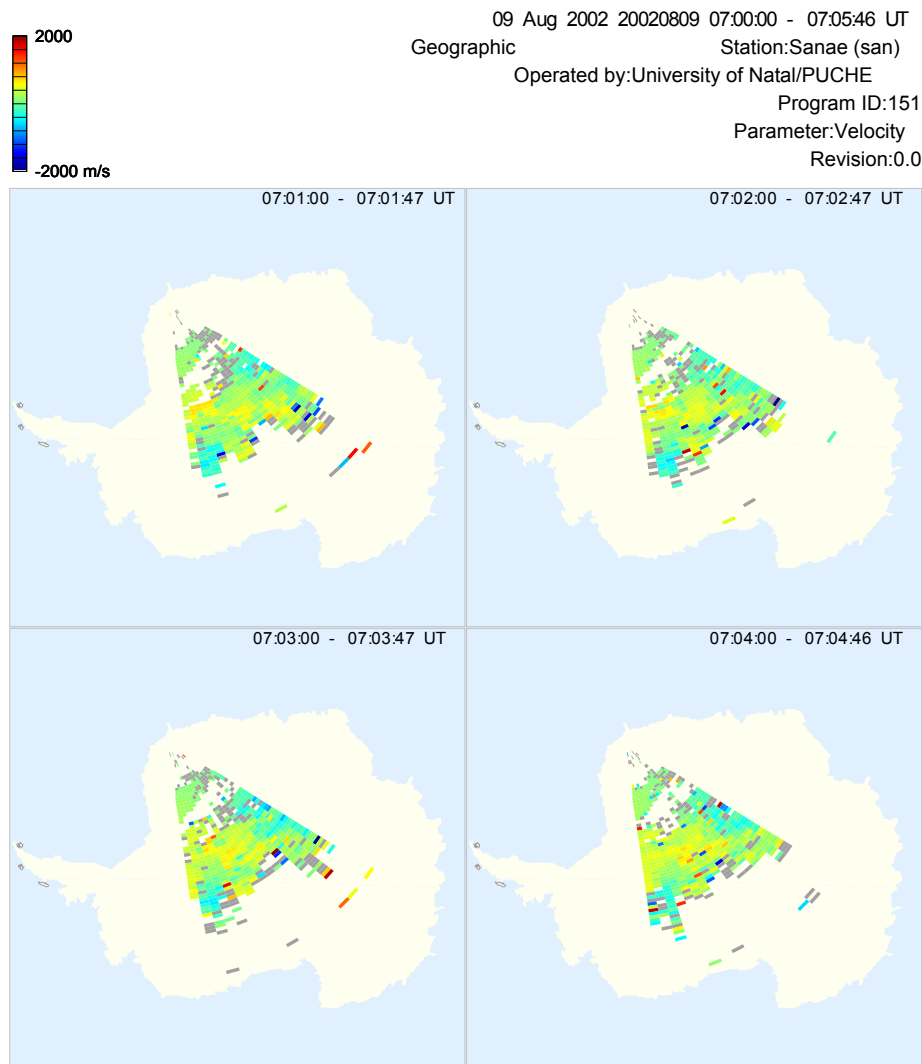


Figure 5.2: Field of view plots show the doppler velocity during the time period 07:01 - 07:05 UT. The plot was produced using SuperDARN data analysis software.

In figure 5.2 the grey colour shows the groundscatter velocity and green to blue colour shows the velocity away from the radar, whereas yellow to red shows the velocity towards the radar. Figure 5.3, shows a summary of generating the time series and the field of view plots. Only the tools that are used in each step are shown.

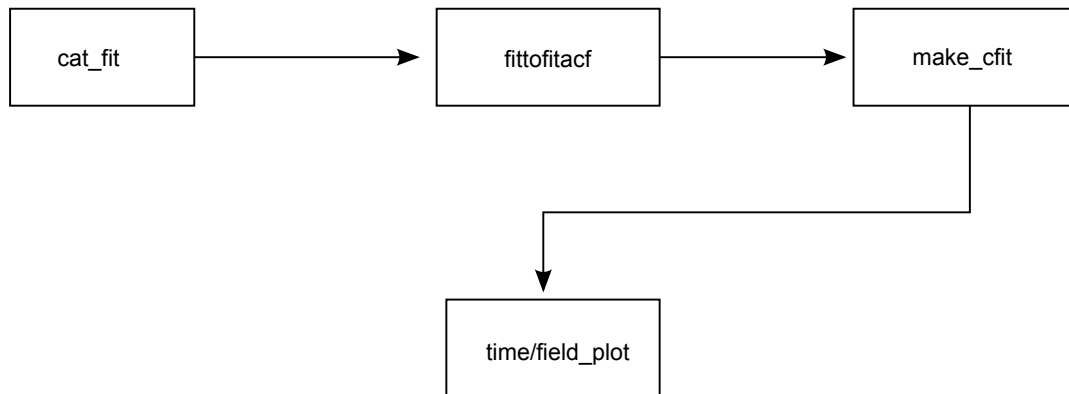


Figure 5.3: Procedure for generating time series and field of view plots

5.1.3 Convection plots

To generate convection maps, data similar to that used in subsection 5.1.1 is used, but this is a multi-step procedure. Since the convection observed by SuperDARN radar depends on the interplanetary magnetic field parameters, the IMF data from the Advanced Composition Explorer (ACE) was used. The step-by-step procedure for generating convection maps follows:

- Step one: concatenate the data from the fit files of each radar to make a data set of 24 hours or one day using tool `cat_fit` [4].
- Step two: convert the fit files into grid files using the tool `make_grid` [4].

The same procedure is applied to each data set of 24 hours data of each radar in the hemisphere of interest.

- Step three: combine the data from all the radars using the tool `combine_grid` [4].

The data from all the radars in the same hemisphere is combined in order to generate the global convection maps [7]. The file name of the new grid file must have SH or NH and the date for identification. NH shows that this is the combined radar data for the northern hemisphere radars and SH for the southern hemisphere radars.

- Step four: convert the grid file generated in step three to empty map file format. Use the tool `map_grid` to convert the grid file to empty map.

The new empty map file has the combined grid files and some empty records. the empty records will be filled when other parameters are added to the file.

- Step five: fill the empty records in the empty map file by adding the Hepner-Maynard boundary [4]. This is the boundary where convection flow is taking place. The tool `map_addhmb` is used.

The file name will change from empty map to hmb map. This helps to identify the next step and the content of the file.

- Step six: add the interplanetary magnetic field data to fill the empty records in the `hmb.map` file. The `hmb.map` file is the same as the empty map file; the name changes after adding/calculating the Hepner-Maynard boundary. The tool `map_addimf` is used to add the interplanetary magnetic field data to the `hmb.map` file [4].

In this step the satellite name, year and delay must be defined so that the software can use the correct data. The satellite data in the `istp` directory must be divided according the name of the satellite and the year [4].

- Step seven: calculate the model vectors using the tool `map_addmodel` [4]. The model has 8 vectors [7].
- Step eight: fit the `model.map` file into the actual convection model using the tool `map_fit` [4].
- Step nine: convert map file into a convection map file using the tool `maptocnvmap` [4]. The `cnvmap` file is used to generate the convection map.
- Step ten: use the tool `map_plot` to plot convection maps [4].

The tool allows one to choose the feature that must appear on the convection map. Figure 5.4 is a summary plot of the procedure of generating convection maps. Only the tool that is used in each step is shown.

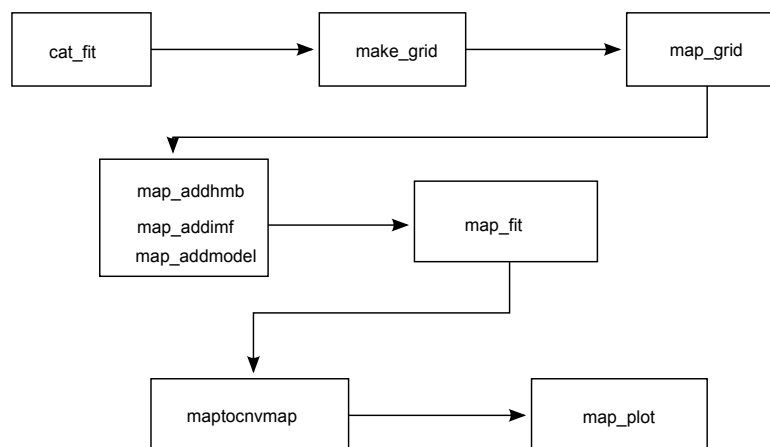


Figure 5.4: Procedure for generating convection maps

Figure 5.5 shows the convection map for the southern hemisphere for the period 00:02 - 00:04 UT. The figure is described in section 5.2. For a detailed description, see appendix A.1.3.

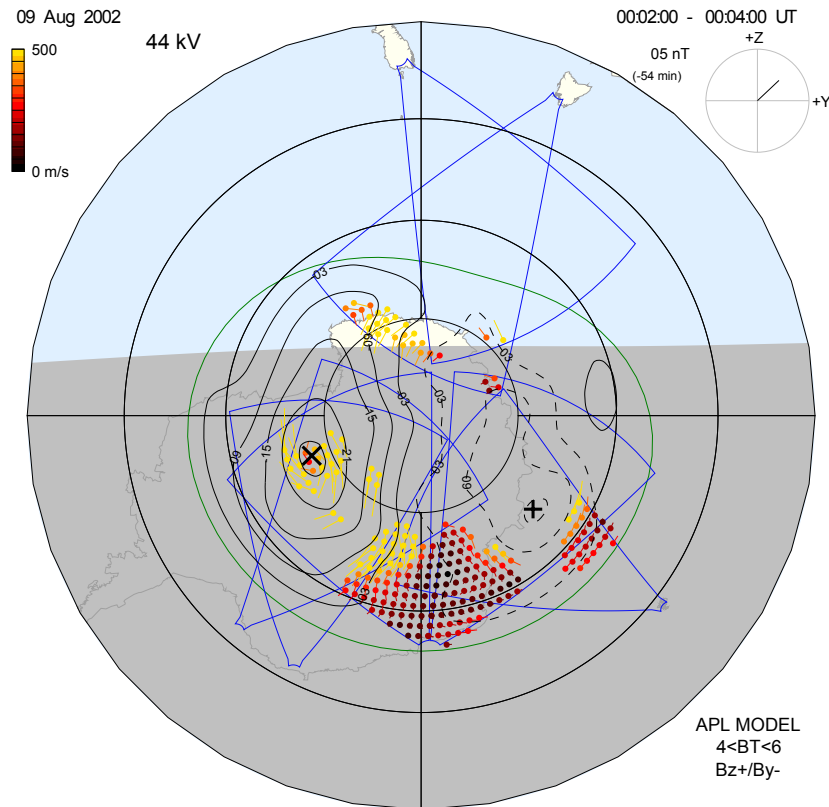


Figure 5.5: Convection map plot showing the convection during the time period 00:02 - 00:04 UT in the southern hemisphere. The plot was produced using SuperDARN data analysis software.

5.2 Convection map orientation

The map orientation is north, which means that we are looking at Antarctica from the inside of the Earth. The dawnside, duskside, noon and midnight are the same as on the northern hemisphere convection map. In figure 5.5 noon is at the top, midnight at the bottom, dusk is at the left and dawn is at the right. The shaded side in figure 5.5 indicates the nightside and the unshaded side is the dayside. The dot represents the cell in which the convection is taking place, the line attached to the dot represents the magnitude and velocity. The magnitude of the velocity is defined in the velocity colour bar on the top left. The number 51 kV on the top left is the cross polar potential and -54 min on the top right of the plot shows the solar wind delay. The interplanetary magnetic field clock angle is on the top right and 06 nT is the total interplanetary magnetic field during the time interval 00:02 - 00:04 UT.

5.3 Conclusion

The plotting produce described in subsections 5.1.1, 5.1.2 and 5.1.3 give an understanding of the backscatter observed by SuperDARN radar in the high-latitude. The direction and the magnitude of the irregularities can be seen in the plots (see figures 5.1, 5.2 and 5.5). The SuperDARN data analysis software is important for generating the interplanetary magnetic field and solar wind plots which help to understand the direction and magnitude of the IMF and the solar wind velocity (see figures 3.7 and 3.8). The orientation of the convection map is north, looking at Antarctica from the inside of the Earth. The duskside, dawnside, noon and midnight are the same as on the northern hemisphere convection map.

Chapter 6

Results

The results presented below are for the events which took place on 09 August 2002 and 30 September 2002. The two days were chosen because of the availability of data from both the spacecraft and SuperDARN radar observed significant backscatter. The Tsyganenko T96 field model was used to map the magnetic footprint of the Cluster spacecraft from space into the ionosphere. If the footprint of the spacecraft was located within the field of view of the SuperDARN radar where the significant backscatter was observed, that event was selected. The SuperDARN radar data presented is from the following radars: Syowa South (69.00°S, 39.58°E) and Syowa East (69.0°S, 39.61°E). We compared the SuperDARN radar and the Cluster spacecraft data.

6.1 Events observed on 09/08/2002

This is a discussion of the observations made by Syowa East SuperDARN radar in the southern hemisphere. On 09 August 2002, the footprint of the Cluster spacecrafts as in figure 6.1 were mapped into the ionosphere using Tsyganenko T96 field model. The Tsyganenko model parameters, interplanetary magnetic field B_y and B_z , disturbed storm index (Dst) and solar wind dynamic pressure (P_{dyn}) were used for the footprint mapping (see table 6.1).

Date	P_{dyn}	Dst	B_y	B_z
09/08/2002	3.443	6.000	4.862	-0.870

Table 6.1: The Tsyganenko field model parameters used to map the Cluster footprint on the 09 August 2002.

The interplanetary magnetic field and solar wind dynamic pressure were obtained from the ACE spacecraft (see figure 6.3). In figure 6.1, the field of view of the Syowa East SuperDARN radar in the southern hemisphere is plotted in red. The green stars represent

the Cluster spacecraft magnetic footprint and the red numbers closer to the stars represent the time (universal time (UT)) in decimal hours.

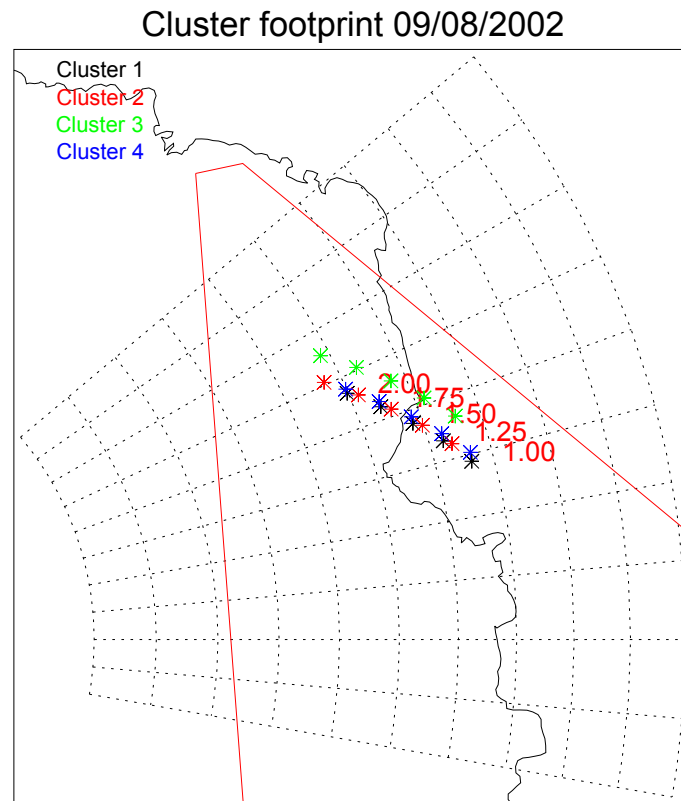


Figure 6.1: Spacecraft magnetic footprint mapped using the Tsyanenko T96 field model. The green stars represent the footprint position, red numbers give universal time (UT) in hours and the triangles represent the field of view of SuperDARN radar in the southern hemisphere.

6.1.1 Observations by the Cluster satellite

At 01 UT the magnetic footprint of the Cluster spacecraft was located within the field of view of the Syowa East SuperDARN radar (see figure 6.1). During this time interval the electric field in the magnetosphere was measured by the Electric Field and Wave form (EFW) instrument on board the Cluster spacecraft. The electric field plots are shown in figure 6.2, the black plot represents Cluster 1 (C1) data, the red plot represents Cluster 2 (C2) data, the green plot represents Cluster 3 (C3) data and the blue plot represents Cluster 4 (C4) data. The duskward electric field is positive and the dawnward electric field is negative. The interplanetary magnetic field during the time of interest is given in figure 6.3.

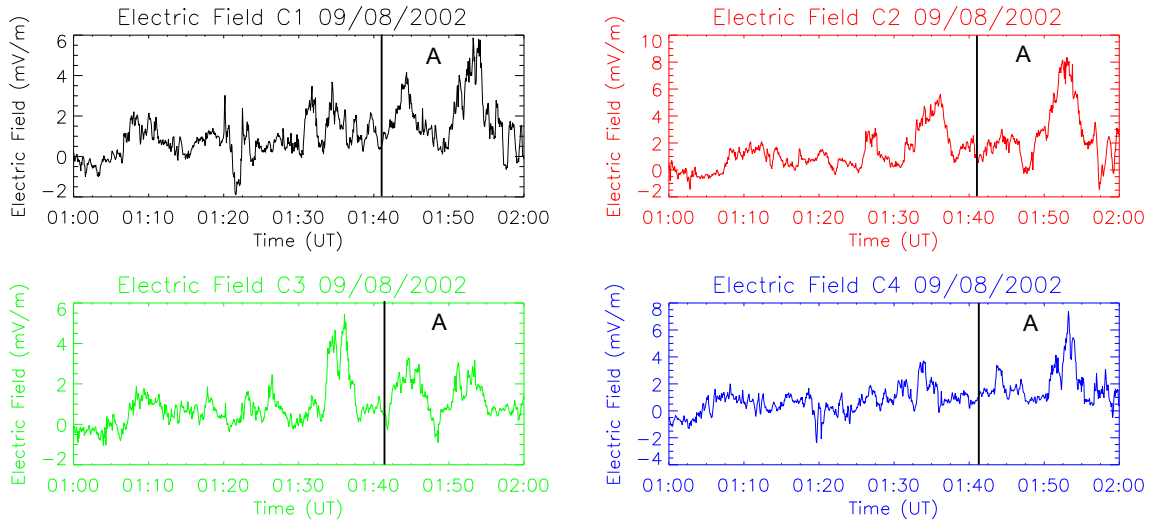


Figure 6.2: The electric field measured by Cluster spacecrafts. The black plot represents Cluster 1 (C1), the red plot represents Cluster 2 (C2), the green plot represents Cluster 3 (C3) and the blue plot represents Cluster 4 (C4). The plots are for the time interval 01:00 - 02:00 UT.

The electric field data used for the event was for the time interval 01:00 UT - 02:00 UT. During the time interval 01:42 - 01:45 UT (A), there was an increase in the duskward electric field for all Cluster spacecrafts and at time 01:45 there was a decrease in the electric field until 01:50 UT (see figure 6.2). During the time interval 01:50 - 01:55 UT there was an increase in the duskward electric field and this increase was followed by a decrease in the electric field observed by all spacecraft at time 01:55 UT (see figure 6.2).

During this time of interest, the interplanetary magnetic field parameters B_x and B_y were negative and their magnitude was close to zero. The B_z interplanetary magnetic field was positive and its magnitude was greater than the B_x and B_y (see figure 6.3). The solar wind propagation delay of ± 54 min was taken into consideration for the generation of convection maps.

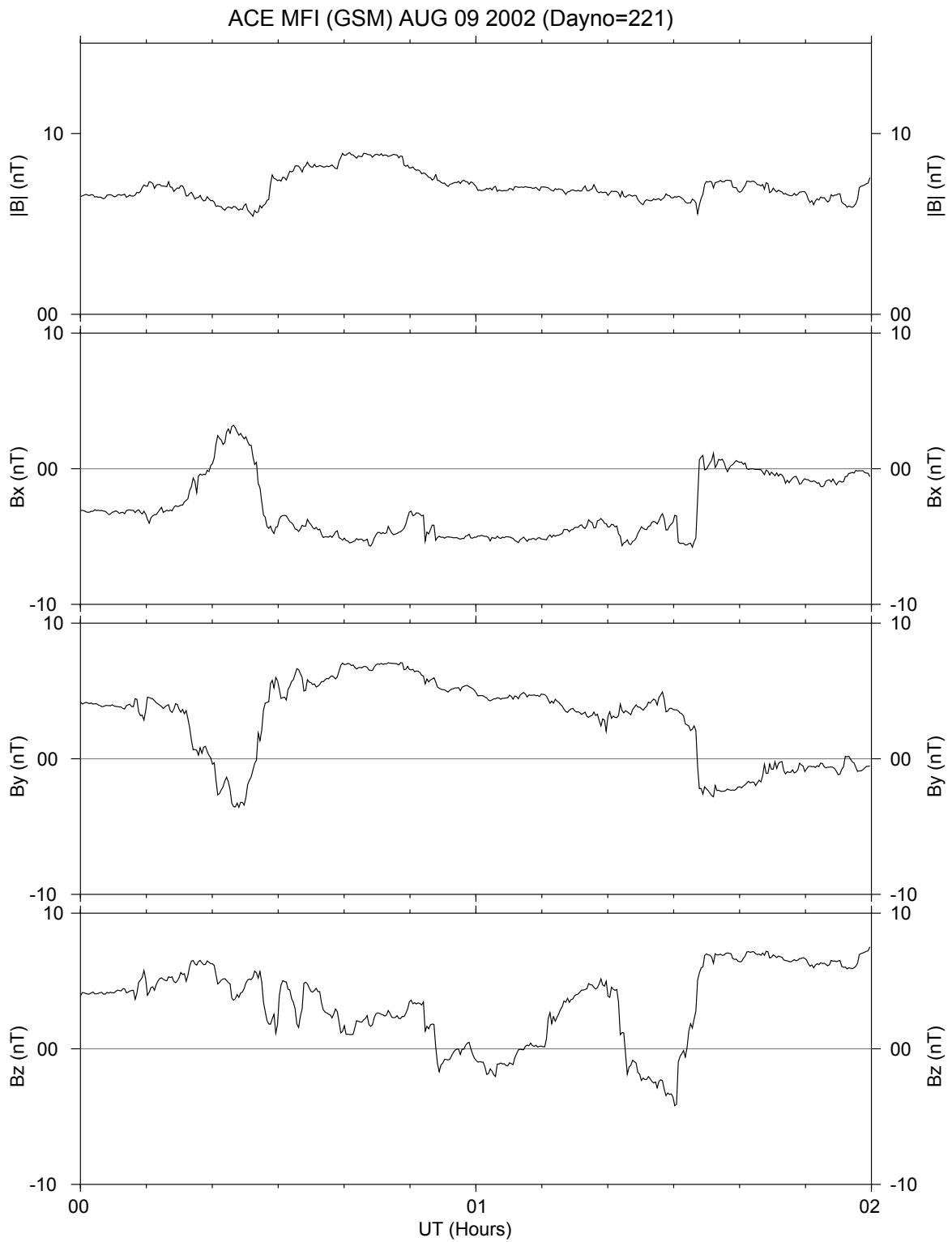


Figure 6.3: Interplanetary magnetic field measured by the ACE spacecraft in Geocentric Solar Magnetic coordinates on 09/08/2002 for the time interval 00 to 02 UT. The plot was produced using SuperDARN toolkit utility `istp_plot`.

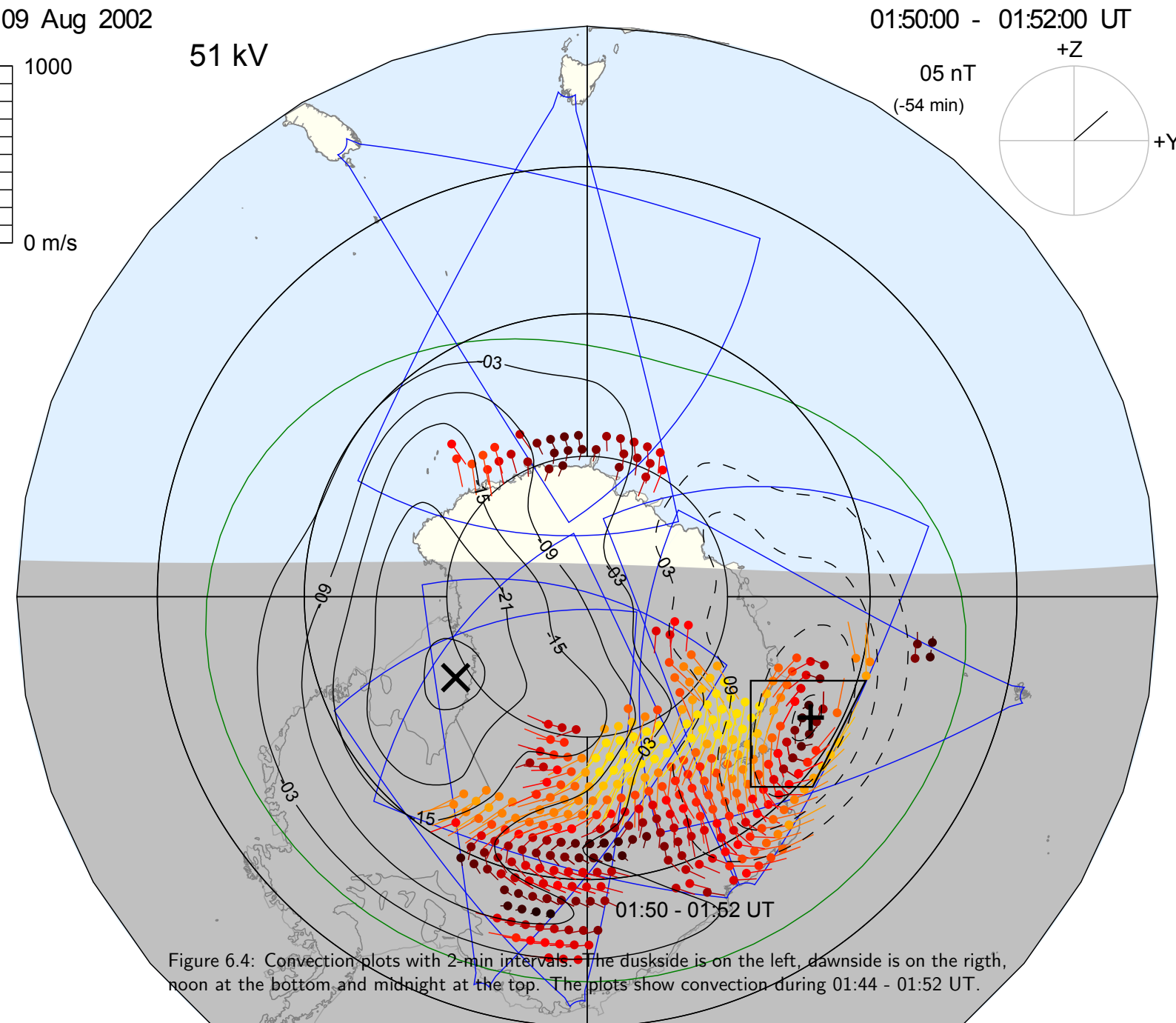
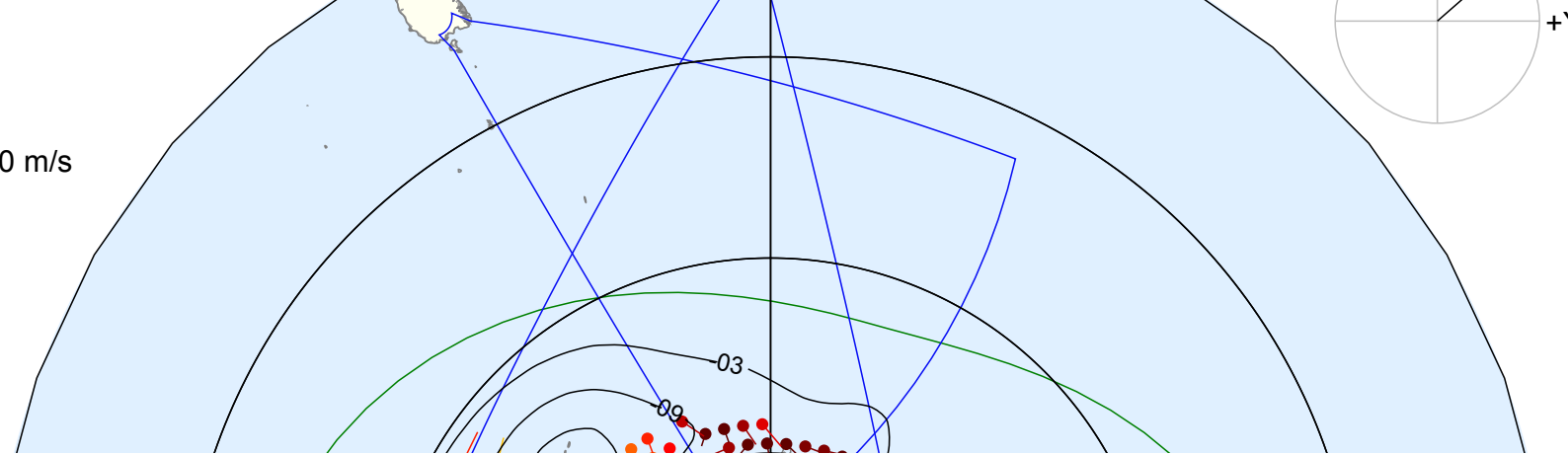
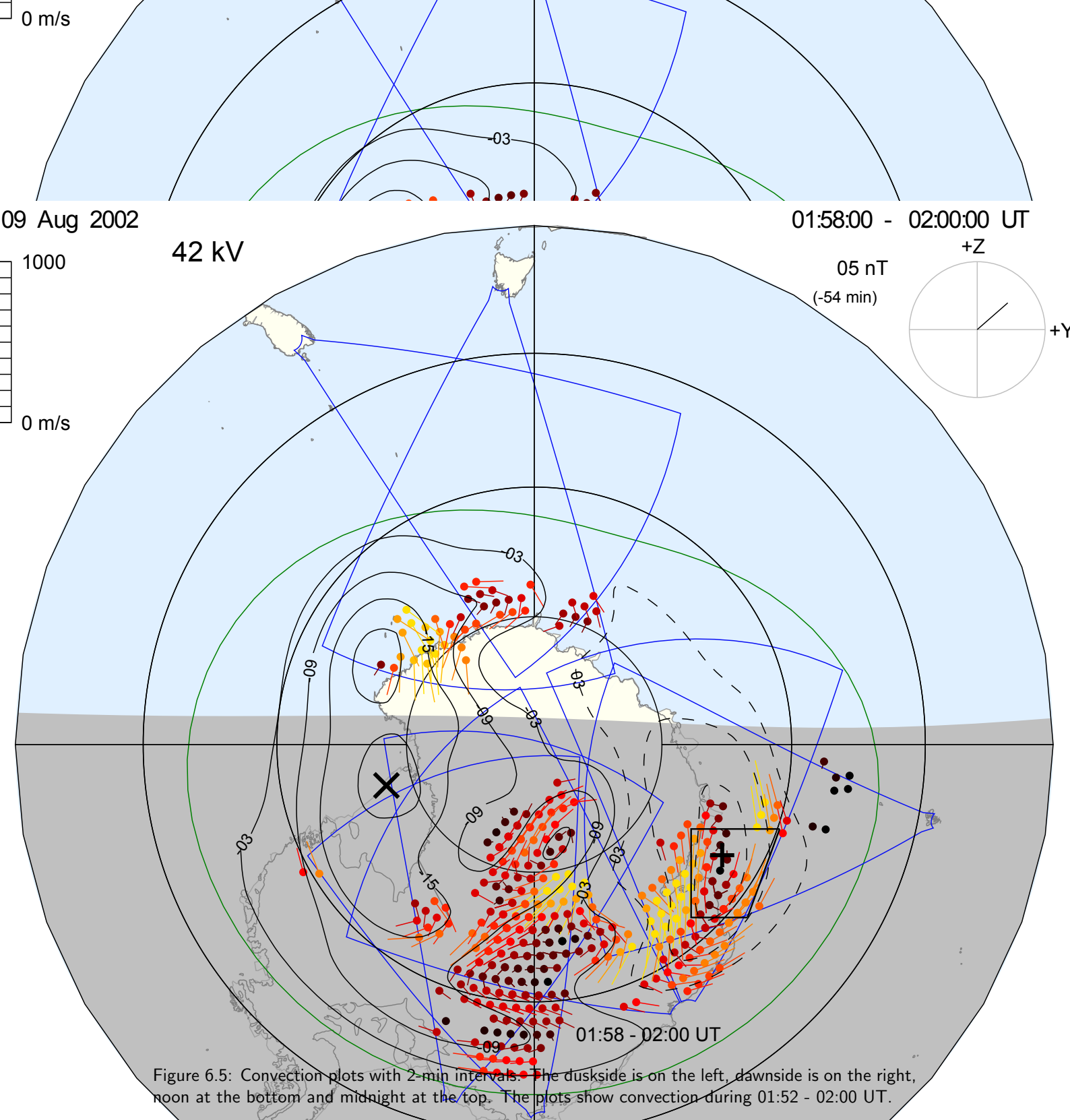


Figure 6.4: Convection plots with 2-min intervals. The duskside is on the left, dawnside is on the right, noon at the bottom and midnight at the top. The plots show convection during 01:44 - 01:52 UT.

The convection time is given at the bottom of each plot. In each convection plot midday is at the top, dawn is on the right, dusk on the left and midnight at the bottom. The dot represents the location where the convection was observed, the line attached to the dot shows the magnitude and the direction of the flow, the colour shows the velocity and the

APL MODEL
 $4 < BT < 6$
 B_z^+ / B_y^-



- During the time interval 01:44 - 01:48 UT a flow from the dayside towards midnight was observed by the SuperDARN radar, and this was a high velocity flow. During this time interval the centre of the convection vortex was in beam 15 of the Syowa East radar and there was less flows towards the dawnside (see figure 6.4).
- From 01:48 - 01:52 UT, the flow started to turn more to the right, the convection vortex centre started to move towards the inside beams and there were more large flows towards the dawnside (see figure 6.4).

APL MODEL
4 < BT < 6
Bz+ / By-

- During the time interval 01:52 - 01:56 UT the radar observed a downward flow, followed by noonward flows (see figure 6.5). During this interval there was a decrease in the midnight flow and strong flows towards the dawnside dominated.
- From 01:56 - 01:58 UT there was strong midnight convection flow and a decrease in the dawnward flow. The centre of the convection vortex started to move to the upper range gates (see figure 6.5). During the time interval 01:58 - 02:00 UT the centre of the convection vortex dropped back to its previous position (range gate) and there was more convection flow towards the dawnside (see figure 6.5).

6.1.3 Comparison of the Cluster and SuperDRN data

At 01:40 UT Cluster observed an increase in the electric field, followed by a decrease in the electric field at 01:45 UT (see figure 6.2). The increase in convection flow and the change in the position of the center of the convection vortex was observed by the SuperDARN radar (see figure 6.4). There was a 4 min time difference between the increase in the electric field and the increase in the convection flow.

When Cluster observed a decrease in the electric field at 01:55 UT, the SuperDARN radar observed a strong dawn to noon convection flow and the centre of the convection vortex dropped to its initial position (See figure 6.5).

6.2 Events observed on 30/09/2002

On 30 September 2002, Syowa South SuperDARN radar in the southern hemisphere observed backscatter velocity from irregularities in the high-latitude ionosphere. During that period the Cluster spacecraft was crossing the field of view of Syowa East SuperDARN radar. The footprint of the Cluster spacecrafts was mapped down into the ionosphere using Tsyganenko T96 field model (see figure 6.6).

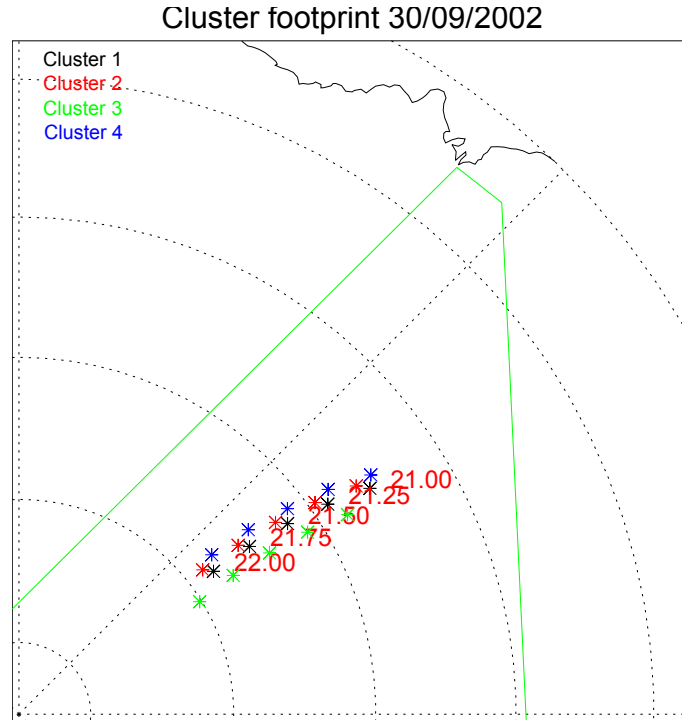


Figure 6.6: Spacecraft magnetic footprint mapped using the Tsyganenko T96 field model. The green stars represent the footprint position, red numbers represent universal time (UT) in hours and the triangle represents the field of view of the SuperDARN radar in southern hemisphere.

The Tsyganenko model parameters, interplanetary magnetic field B_y and B_z , disturbed storm index (Dst) and solar wind dynamic pressure (P_{dyn}) were used for the footprint mapping (see table 6.2).

Date	P_{dyn}	Dst	B_y	B_z
30/09/2002	8.66	-12.000	-18.265	16.784

Table 6.2: The Tsyganenko field model parameters used to map the Cluster footprint on the 30 September 2002.

The interplanetary magnetic field was obtained from ACE spacecraft and the solar-wind propagation delay of ± 54 min was taken into consideration for the generation of convection maps (see figure 6.7). The field of view of Syowa South SuperDARN radar in southern hemisphere is plotted in green (see figure 6.6).

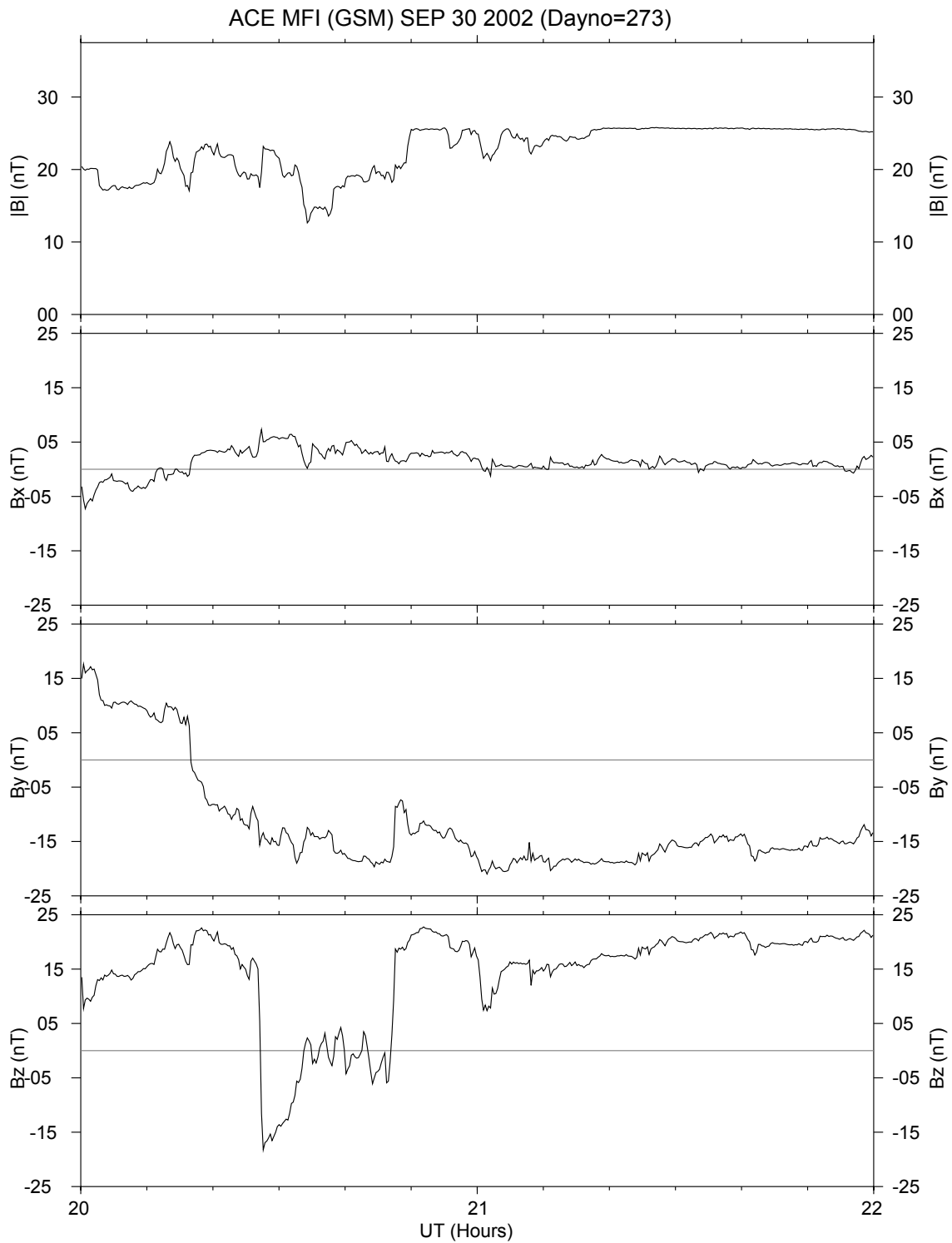


Figure 6.7: Interplanetary magnetic field measured by ACE spacecraft in Geocentric Solar Magnetic coordinates on the 30-09-2002 for the time interval 20:00 - 22:00 UT. The plot was produced using SuperDARN toolkit utility `istp_plot`.

6.2.1 Observations by the Cluster satellite

At 21 UT the magnetic footprint of the Cluster spacecraft was located within the field of view of the Syowa South SuperDARN radar, see figure 6.6. At that time the electric field in the magnetosphere was measured by the Electric Field and Wave form (EFW) instrument on board the Cluster spacecraft. The electric field plots are shown in figure 6.8, and the spacecrafts data representation is the same as figure 6.2. The duskward electric field is positive and the dawnward electric field is negative. The interplanetary magnetic field during the time of interest is given in figure 6.7.

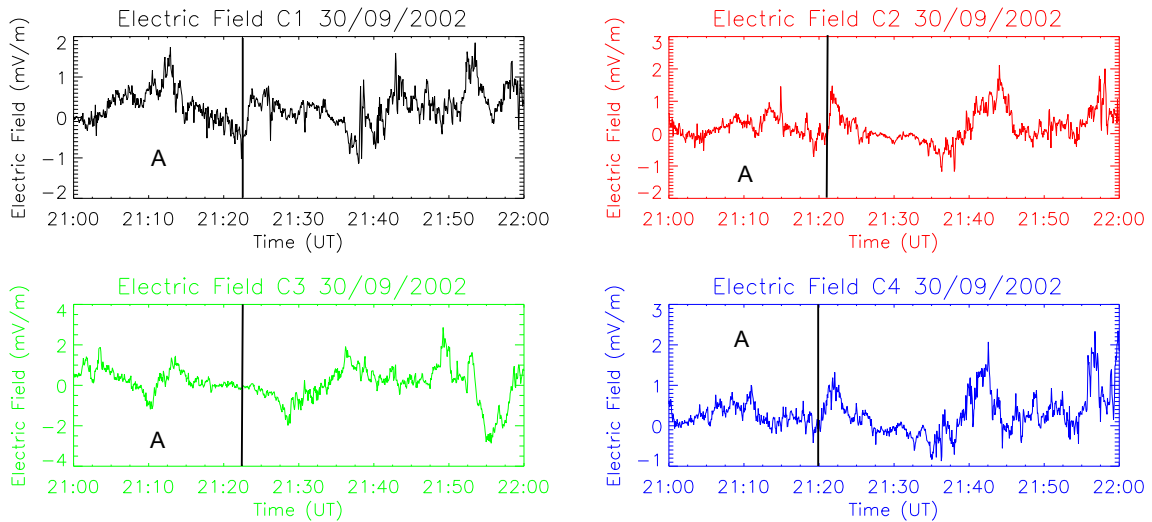


Figure 6.8: The electric field measured by the Cluster spacecrafts. The black plot represents from Cluster 1 (C1), red plot represents from Cluster 2 (C2), green plot represents from Cluster 3 (C3) and blue plot represents from Cluster 4 (C4).

The electric field data in figure 6.8 shows a gradual increase in the electric field in the duskside between 21:00 UT and 21:12 UT. At 21:12 UT there was a gradual decrease in the electric field from the duskside towards the dawnside (see figure 6.8). The larger increase in electric field was observed by Cluster 1 and Cluster 3. The increase observed by Cluster 3 took place earlier than the one observed by Cluster 1 (see figure 6.8). The interplanetary magnetic field during this period of interest was obtained from the ACE spacecraft. During this period the B_x and B_y parameters of the interplanetary magnetic field were positive and the B_z parameter was initially negative but it turned positive during the time of interest (A) (see figure 6.7).

6.2.2 Observations by the SuperDARN radar

When the Cluster spacecraft observed the electric field in the magnetosphere, the Syowa South SuperDARN radar observed the backscatter velocity from the irregularities in the upper ionosphere. In figure 6.9, four convection plots are shown with 2 min intervals between the plots.

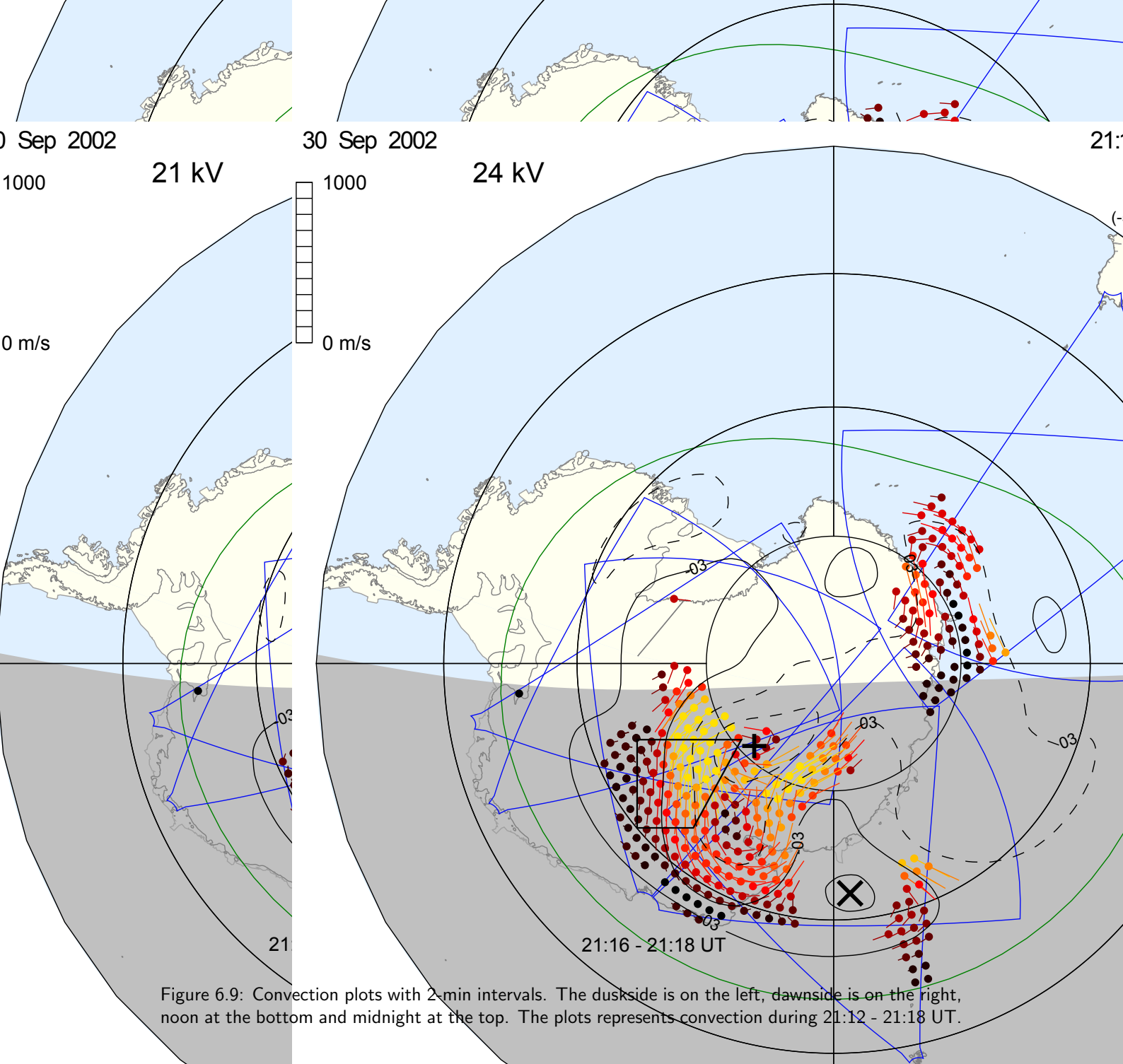


Figure 6.9: Convection plots with 2-min intervals. The duskside is on the left, dawnside is on the right, noon at the bottom and midnight at the top. The plots represents convection during 21:12 - 21:18 UT.

The convection time is given on the bottom of each plot. In figure 6.9 midday is at the top, dawn is on the right, dusk on the left and midnight at the bottom.

- During the time interval 21:10 - 21:12 UT SuperDARN radar observed a convection flow of small magnitude towards midnight (see figure 6.9).
- The change in convection flow from small to very large flow was observed by the radar between 21:12 UT and 21:18 UT (see figure 6.9).
- From 21:20 - 21:22 UT the convection flow towards midnight started to turn dawnward and the flow magnitude become smaller.

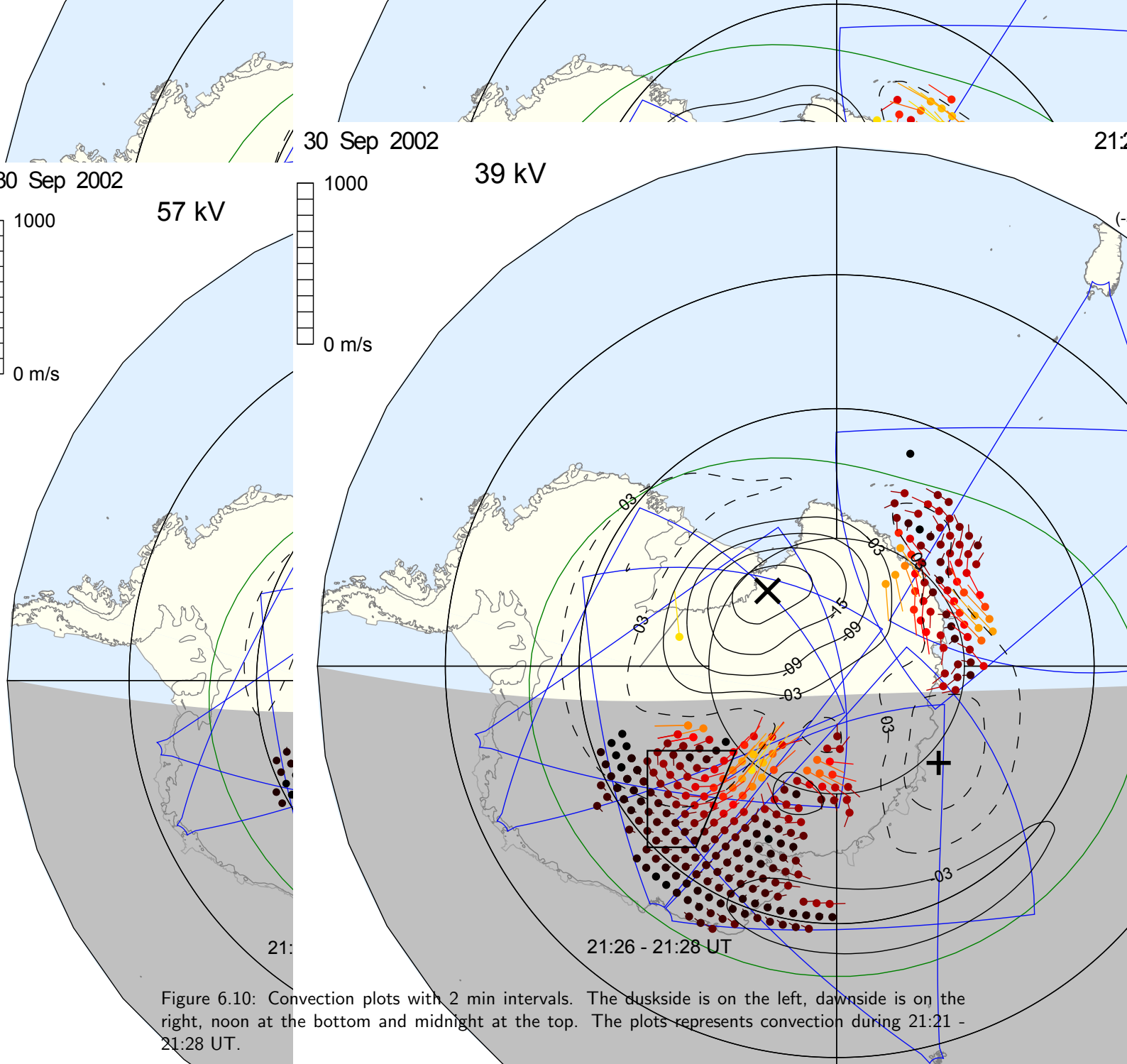


Figure 6.10: Convection plots with 2 min intervals. The duskside is on the left, dawnside is on the right, noon at the bottom and midnight at the top. The plots represents convection during 21:21 - 21:28 UT.

- From 21:22 - 21:24 UT there was a strong flow towards midnight and this flow was followed by weak flow towards the dawnside (see figure 6.10).
- During the time interval 21:24 - 21:28 UT there was a decrease in the convection flow and the convection direction tilted towards the dawnside (see figure 6.10).

6.2.3 Comparison of the Cluster and SuperDRN data

During 21:02 - 21:12 UT the Cluster spacecrafts observed an increase in electric field (see figure 6.8). From 21:10 - 21:12 UT SuperDARN radar observed a small convection flow from noon to midnight, followed by increase in convection flow during the time period 21:12 - 21:18 UT (see figure 6.9).

During the time period 21:12 - 21:22 UT Cluster observed a decrease in electric field (see figure 6.8). The SuperDARN radar observed a decrease in the convection flow between the time period 21:20 and 21:28 UT. The time delay between the changes in Cluster and SuperDARN was also observed.

6.3 Conclusion

When Cluster observed change in the electric field, SuperDARN radar observed variations in convection flow (see figures 6.2 and 6.8). Changes in the electric field also affected the position of the centre of the convection vortex (see figures 6.4 and 6.5) and the magnitude and direction of the convection flow (see figures 6.9 and 6.10).

Chapter 7

Discussion and Conclusion

The objectives of this study, as discussed in chapter 1, were met using Advanced Composition Explorer (ACE), Cluster and SuperDARN radar data. The Tsyganenko T96 field model was used to map the events taking place in the magnetosphere into the ionosphere and SuperDARN data analysis software was used to plot and interpret the radar observations in the high-latitude ionosphere.

The Tsyganenko field model proved to be reliable model for mapping points in space into the ionosphere. The model is able to map and trace field lines from the magnetosphere regions into the ionosphere (see figures 2.8 and 2.9). The correct input parameters play an important role for the model to perform optimally. The Tsyganenko T96 field model uses the following parameters: interplanetary magnetic field (B_y and B_z), disturbed storm index (Dst) and solar wind dynamic pressure (P_{dyn}).

Figures 2.8 (parallel) and (anti-parallel) show a field line which was traced from point X in the magnetosphere into the ionosphere. Figure 2.8 (parallel) shows the field which was traced from point X in the magnetosphere into the northern hemisphere ionosphere and figure 2.8 (anti-parallel) shows the field line which was traced from point X in the magnetosphere into the southern hemisphere ionosphere. The field line coordinates in the northern hemisphere calculated by the model was used to trace the field from point X in the northern hemisphere into the southern hemisphere ionosphere. Figure 2.8 (bottom) shows that the spacecraft was crossing a closed field line.

Figure 2.9 (B) and figure 6.1 the two figures show the Cluster spacecraft position on the 09/08/2002. In figure 2.9 the quiet day input parameters were used to map the magnetic footprint of Cluster into the ionosphere ($B_y = 0$, $B_z = 0$, $Dst = 0$ and $P_{dyn} = 2$). In figure 6.1 the real time data input parameters of interplanetary magnetic field (B_y and B_z) and solar wind dynamic pressure (P_{dyn}) from the ACE satellite were used. The position of the footprint at 1 UT in both figures changes when real time data is used.

The SuperDARN data analysis software was used in this study to generate the interplanetary magnetic field, time series, field of view and convection plots. The time series plot

can be used to identify the beam where more backscatter was observed and it is much easier to identify ground scatter using the time series plot. It also important to identify the range in which large velocity flow takes place (see figure 5.1) and the plot can zoom into the range, time and beam of interest. The field of view plot can be used to see how the radar observed the backscatter during a certain period time. It also make it possible to see how the backscatter changes along the ranges of beams of the radar (see figure 5.2).

The convection map can be used to identify the regions where large convection is taking place. The convection map shows the direction and the magnitude of the flow and it gives information on the solar wind parameters during the time for which the plot was generated. This includes the polar cap potential (see figure 5.5). To generate the convection map using a SuperDARN data analysis software is a multi-step process (see figure 5.4). The file format `cnvmap` is used to generate the convection map.

Events that took place on 09/08/2002 and 30/09/2002 were analysed. The magnetospheric data from Cluster and high-latitude ionospheric data from SuperDARN radar were used for this analysis. The electric field measured by the Electric Field and Wave form instrument on board the Cluster spacecraft and the convection flow observed by SuperDARN radars were compared.

On the 09/08/2002 the Cluster spacecraft footprint was located within the field of view of the Syowa East SuperDARN radar (see figure 6.1). The Tsyganenko T96 field model was used to map the footprint into the ionosphere. An increase in the electric field was observed by Cluster at 01:40 UT and this increase was followed by a decrease in the electric at 01:45 UT. At 1:50 UT Cluster observed an increase in the electric field and at 01:55 the electric field start to decrease (see figure 6.2).

During the time interval 01:40 - 02:00 UT the interplanetary magnetic field parameters B_x and B_y were negative and a strong positive B_z interplanetary magnetic field was measured by ACE (see figure 6.3). The SuperDARN radar observed a large convection flow towards midnight during the time interval 1:44 - 1:50 UT. During this interval the convection vortex centre which was initially at beam 15, started to move towards the inner beams (see figure 6.4). During the time interval 1:52 - 2:00 UT the convection flow decreased and dawnward flows were observed near the centre of the convection vortex (see figure 6.5).

On the 30/09/2002 the Cluster spacecraft footprint position was mapped within the field of view of the Syowa South SuperDARN radar by means of the Tsyganenko field model (see figure 6.6). The electric field data during the time interval 21:00 - 21:12 UT shows an increase in the electric field, followed by a gradual decrease in the electric field during the time interval 21:12 - 21:22 UT (see figure 6.8). The SuperDARN radar observed an increase in the convection flow during the time interval 21:10 - 21:18 UT (see figure 6.9), followed by a decrease in the convection flow during the time interval 21:20 UT (see figure 6.10).

Cluster and SuperDARN radar data, show that a change in the electric field measured by

Cluster, is followed by a change in the convection flow as observed by the radar. These changes don't take place simultaneously. There is a time delay from the time Cluster observes a change until the time SuperDARN observes a change. Looking at the two events presented in this study, it can be said that the change in convection flow observed by SuperDARN radar results from the change in the electric field.

7.1 Future work

Data from SuperDARN radar and the Electric Field and Wave instrument was used in this study. Since plasma in the ionosphere is composed of ions and electrons, the data from other instrument in the Cluster spacecraft can also be used to confirm the observations made by the EFW instrument and SuperDARN, e.g the Electron Drift instrument (EDI), WHISPER and CIS instruments. The electric field and velocity of electrons measured by EDI can be compared with the EFW electric field and SuperDARN radar data.

Multi-instrument measurements can also be done using SuperDARN radar, low orbit satellite, and Cluster and the data from the instruments can be compared. Modeling of the electric fields allows a more quantitative analysis of the events presented in this thesis. This can be achieved using the electric field and magnetic field measured by Cluster to derive the velocity of plasma in space and also in the ionosphere. The ionospheric velocity derived from electric field (EFW) and magnetic field (FGM) Cluster data and the velocity observed by SuperDARN radar can be compared.

Appendix A

SuperDARN data analysis software

A.1 SuperDARN data analysis software

The SuperDARN toolkit is a data analysis software package which was developed by Rob Barnes for the users of SuperDARN radar data. The software consists of different tools capable of analysing and generating plots, such as interplanetary magnetic field, vector and convection plots. The software is available on the SuperDARN website [3]. For more discussion of the software see [3] and [4].

A.1.1 Time series plots

The procedure for generating a time series plot is as follows:

- Step one: concatenate the data from fit files of each radar to make a data set 24 hours or one day using tool `cat_fit` [4].

```
cat_fit fname00 fname02 . . . fname22 fnameoutput
```

```
ca_fit 2002080900d.fit 2002080902d.fit . . . 2002080922d.fit 20020809d.fit
```

where `fname` is file name and each file starts with four digits representing year, followed by two digits for months, followed by two for day and the last two digits representing time in hours. The alphabet letter represent the radar code. For more information on radar code see [7].

- Step two: convert the 24 hours fit file generated in step one, into `fitacf` using the tool `fittofitacf` [4].

```
fittofitacf fname.fit > fname.fitacf
```

```
fittofitacf 20020809d.fit > 20020809d.fitacf
```

- Step three: compress the fitacf to form cfit file using the tool `make_cfit` [4]. The cfit file is used to generate a time series plot.

```
make_cfit -new -p min fname.fitacf > fname.cfit
```

```
make_cfit -new -p 0.0 20020809d.fitacf > 20020809d.cfit
```

where `-p` stand for the minimum power and `-new` option mean the file must be in a new dmap base. dmap is the file generated by software to store gridded data.

- Step four: use the `time_plot` tool to plot the time series plot [4].

```
time_plot -cfit -x -my options fname.cfit
```

```
time_plot -cfit -x -my options 20020809d.cfit
```

where `-cfit` show that the data is in cfit format and `-my` option is the script which has the features that must appear on the plot, features such as beam number, range and time of interest, etc.

A.1.2 Field of view plots

The procedure for generating field of view plot is as follows:

- Step one: concatenate the data from the fit files of each radar to make a data set of 24 hours or one day using tool `cat_fit` [4].

```
cat_fit fname00 fname02 . . . fname22 fnameoutput
```

```
ca_fit 2002080900d.fit 2002080902d.fit . . . 2002080922d.fit 20020809d.fit
```

where `fname` is file name and each file starts with four digits representing year, followed by two digits for months, followed by two for day and the last two digits representing time in hours. The alphabet letter represents the radar code. For more information on radar code see [7].

- Step two: convert the 24 hours fit file generated in step one into fitacf using the tool `fittofitacf` [4].

```
fittofitacf fname.fit > fname.fitacf
```

```
fittofitacf 20020809d.fit > 20020809d.fitacf
```

- Step three: compress the fitacf to form cfit file using the tool `make_cfit` [4].

```
make_cfit -new -p min fname.fitacf > fname.cfit
```

```
make_cfit -new -p 0.0 20020809d.fitacf > 20020809d.cfit
```

where `-p` stand for the minimum power and `-new` option mean the file must be in a new dmap base. `dmap` is the file generated by the software to store gridded data.

- Step four: use the tool `field_plot` to generate a field of view plot [4].

```
field_plot -cfit -x -my options fname.cfit
```

```
field_plot -cfit -x -my options 20020809d.cfit
```

where `-my options` is similar to the one used in the time series plot, but in the field of view plot you choose whether you want to plot the power, velocity or spectral width.

A.1.3 Convection plots

The procedure followed to generate convection maps:

- Step one: concatenate the data from the fit files of each radar to make a data set of 24 hours or one day using tool `cat_fit` [4].

```
cat_fit fname00 fname02 . . . fname22 fnameoutput
```

```
ca_fit 2002080900d.fit 2002080902d.fit . . . 2002080922d.fit 20020809d.fit
```

where `fname` is file name and each file starts with four digits representing year, followed by two digits for months, followed by two digits for day and the last two digits representing time in hours. The alphabet letters represent the radar code.

- Step two: convert the fit files into grid files using the tool `make_grid` [4].

```
make_grid fname.fit > fname.grd
```

```
make_grid 20020809d.fit > 20020809d.grd
```

the same procedure is applied for all 24 hours data of each radar in the hemisphere of interest.

- Step three: combine the data from all the radars using the tool `combine_grid` [4].

```
combine_grid fname.grd1 fname.grd2 . . . > fname.grd
```

```
combine_grid 20020809d.grd 20020809h.grd . . . > 20020809.grd
```

where `fname.grd1` represents the data file from radar one, `fname.grd2` represents the data file from radar 2 and `fname.grd` will be the new data file with the data from all radars in that hemisphere.

- Step four: use the tool `map_grid` to convert the grid file to empty map.

```
map_grid fname.grd > fname.empty.map
```

```
map_grid 20020809.grd > 20020809.empty.map
```

- Step five: use the tool `map_addhmb` to add the Hepner-Maynard boundary into the empty map file.

```
map_addhmb fname.empty.map > fname.hmb.map
```

```
map_addhmb 20020809.empty.map > 20020809.hmb.map
```

- Step six: use the tool `map_addimf` to add the interplanetary magnetic field data in the `hmb.map` file [4].

```
map_addimf -satellite -year -delay fname.hmb.map > fname.imf.map
```

```
map_addimf -ace 2002 -d 0:54 20020809.hmb.map > 20020809.imf.map
```

- Step seven: use the tool `map_addmodel` to calculate the model vectors [4].

```
map_addmodel -number of coefficients fname.imf.map > fname.model.map
```

```
map_addmodel -o 8 20020809.imf.map > 20020809.model.map
```

- Step eight: fit the `model.map` file into the actual convection model using the tool `map_fit` [4].

```
map_fit fname.model.map > fname.map
```

```
map_fit 20020809.model.map > 20020809.map
```

- Step nine: use the tool `maptocnvmap` to convert map file into a convection map file the tool [4].

```
maptocnvmap fname.map > fname.cnvmap
```

```
maptocnvmap 20020809.map > 20020809.cnvmap
```

- Step ten: use the tool `map_plot` to plot convection maps [4].

```
map_plot -x -my options fname.cnvmap
```

```
map_plot -x -my options 20020809.cnvmap
```

where `-x` shows that the convection maps will appear on the screen and are not going to be saved on the computer. If you want to save them on the computer you replace `-x` with `-PS`. When the `-PS` command is used, the postscripted images will be produced and saved in the RST directory.

References

- [1] <http://ccmc.gsfc.nasa.gov/modelweb/magnetos/igrf.html>.
- [2] <http://helios.gsfc.nasa.gov/magneto.jpeg>.
- [3] <http://superdarn.jhuapl.edu>.
- [4] <http://superdarn.jhuapl.edu/doc/tutorial>.
- [5] O. Amm, E. F. Donovan, H. Frey, M. Lester, R. Nakamura, J. A. Wild, A. Aikio, M. Dunlop, K. Kauristie, A. Marchaudon et al. Coordinated studies of the geospace environment using Cluster, satellite and ground-based data: an interim review. *Ann. Geophys.*, 23(6):2129–2170, 2005.
- [6] G. Chisham, M. P. Freeman, T. Sotirelis and R. A. Greenwald. The accuracy of using the spectral width boundary measured in off-meridional SuperDARN HF radar beams as a proxy for the open-closed field line boundary. *Ann. Geophys.*, 23(7):2599, 2005.
- [7] G. Chisham, M. Lester, S. E. Milan, M. P. Freeman, W. A. Bristow, A. Grocott, K. A. McWilliams, J. M. Ruohoniemi, T. K. Yeoman, P. L. Dyson et al. A decade of the Super Dual Auroral Radar Network (SuperDARN): scientific achievements, new techniques and future directions. *Surv. Geophys.*, 28(1):33–109, 2007.
- [8] P. T. I. Eriksson, L. G. Blomberg, A. D. M. Walker and K. Glassmeier. Poloidal ULF oscillations in the dayside magnetosphere: a Cluster study. *Ann. Geophys.*, 23(7):2679, 2005.
- [9] C. P. Escoubet, R. Schmidt and M. L. Goldstein. Cluster–science and mission overview. *Space Sci. Rev.*, 79(1):11–32, 1997.
- [10] D. H. Fairfield. An evaluation of the Tsyganenko magnetic field model. *J. Geophys. Res. (Space Physics)*, 96(A2):1481–1494, 1991.
- [11] R. A. Greenwald, K. B. Baker, J. R. Dudeney, M. Pinnock, T. B. Jones, E. C. Thomas, J. P. Villain, J. C. Cerisier, C. Senior, C. Hanuise et al. DARN/SuperDARN. *Space Sci. Rev.*, 71(1):761–796, 1995.

- [12] A. Grocott, T. K. Yeoman, S. E. Milan, O. Amm, H. U. Frey, L. Juusola, R. Nakamura, C. J. Owen, H. Rème and T. Takada. Multi-scale observations of magnetotail flux transport during IMF-northward non-substorm intervals. *Ann. Geophys.*, 25(7):1709–1720, 2007.
- [13] A. Grocott, T. K. Yeoman, S. E. Milan and S. W. H. Cowley. Interhemispheric observations of the ionospheric signature of tail reconnection during IMF-northward non-substorm intervals. *Ann. Geophys.*, 23(5):1763–1770, 2005.
- [14] G. Gustafsson, R. Boström, B. Holback, G. Holmgren, A. Lundgren, K. Stasiewicz, L. Åhlén, F. S. Mozer, D. Pankow, P. Harvey et al. The electric field and wave experiment for the Cluster mission. *Space Sci. Rev.*, 79(1):137–156, 1997.
- [15] K. Kabin, R. Rankin, G. Rostoker, R. Marchand, I. Rae, A. J. Ridley, T. I. Gombosi, C. R. Clauer and D. L. DeZeeuw. Open-closed field line boundary position: A parametric study using an MHD model. *J. Geophys. Res. (space physics)*, 109, 2004.
- [16] M. G. Kivelson and C. T. Russell. *Introduction to space physics*. Cambridge University Press, 1995.
- [17] A. V. Koustov, D. W. Danskin, R. A. Makarevitch and J. D. Gorin. On the relationship between the velocity of E-region HF echoes and $E \times B$ plasma drift. *Ann. Geophys.*, 23(2):371–378, 2005.
- [18] R. A. Langel, R. H. Estes and G. D. Mead. Some new method in geomagnetic field modeling applied to the 1960-1980 epoch. *J. Geomag. Geoelectr.*, 34:327–349, 1982.
- [19] M. Lockwood, H. Opgenoorth, A. Van Eyken, A. Fazakerley, J. Bosqued, W. Denig, J. Wild, C. Cully, R. Greenwald, G. Lu et al. Coordinated Cluster, ground-based instrumentation and low-altitude satellite observations of transient poleward-moving events in the ionosphere and in the tail lobe. *Ann. Geophys.*, 19:1589–1612, 2001.
- [20] L. R. Lyons and D. J. Williams. *Quantitative aspects of magnetospheric physics*. Springer, 1984.
- [21] M. Manda and S. Macmillan. International geomagnetic reference field - the eighth generation. *Earth Planets Space.*, 52(12):1119–1124, 2000.
- [22] A. Marchaudon, J. C. Cerisier, J. M. Bosqued, M. W. Dunlop, J. A. Wild, P. Décréau, M. Förster, D. Fontaine and H. Laakso. Transient plasma injections in the dayside magnetosphere: one-to-one correlated observations by Cluster and SuperDARN. *Ann. Geophys.*, 22(1):141–158, 2004.
- [23] M. Marcucci, I. Coco, D. Ambrosino, E. Amata, S. Milan, M. Cattaneo and A. Retinò. Extended SuperDARN and IMAGE observations for northward IMF: Evidence for dual lobe reconnection. *J. Geophys. Res.*, 113(A2):A02204, 2008.

- [24] K. A. McWilliams, G. J. Sofko, T. K. Yeoman, S. E. Milan, D. G. Sibeck, T. Nagai, T. Mukai, I. J. Coleman, T. Hori and F. J. Rich. Simultaneous observations of magnetopause flux transfer events and of their associated signatures at ionospheric altitudes. *Ann. Geophys.*, 22(6):2181–2199, 2004.
- [25] G. D. Mead and D. H. Fairfield. A quantitative magnetospheric model derived from spacecraft magnetometer data. *J. Geophys. Res. (space physics)*., 80:523–534, 1975.
- [26] S. H. Mthembu. An investigation of ultra low frequency (ULF) pulsations using radar and solar wind data. Master’s thesis, School of Physics University of Kwazulu-Natal Durban, 2006.
- [27] T. Ondoh and T. Marubashi. *Science of Space Environment*. IOS Press., 2001.
- [28] J. M. Ruohoniemi and R. A. Greenwald. Dependencies of high-latitude plasma convection: Consideration of interplanetary magnetic field, seasonal, and universal time factors in statistical patterns. *J. Geophys. Res. (Space Physics)*., 110(A9):A09204, 2005.
- [29] E. C. Stone, A. M. Frandsen, R. A. Mewaldt, E. R. Christian, D. Margolies and J. F. Ormes. Snow. F., The Advanced Composition Explorer. *Space Sci. Rev.*, 86:1–22, 1998.
- [30] J. R. Taylor, S. W. H. Cowley, T. K. Yeoman, M. Lester, T. B. Jones, R. A. Greenwald, G. Sofko, J. P. Villain, R. P. Lepping and M. R. Hairston. SuperDARN studies of the ionospheric convection response to a northward turning of the interplanetary magnetic field. *Ann. Geophys.*, 16(5):549–565, 1998.
- [31] N. A. Tsyganenko. Modeling the earth’s magnetospheric magnetic field confined within a realistic magnetopause. *J. Geophys Res. (Space Physics)*., 100:5599–5612, 1995.
- [32] N. A. Tsyganenko. Effects of the solar wind conditions on the global magnetospheric configuration as deduced from data-based field models. In *Third International Conference on Substorms (ICS-3), Versailles, France*, 1996.
- [33] A. D. M. Walker. The SHARE Radar at SANAE, Antarctica. *SAJS.*, 98:257 – 263, 2002.
- [34] J. A. Wild, S. W. H. Cowley, J. A. Davies, H. Khan, M. Lester, S. E. Milan, G. Provan, T. K. Yeoman, A. Balogh, M. W. Dunlop et al. First simultaneous observations of flux transfer events at the high-latitude magnetopause by the Cluster spacecraft and pulsed radar signatures in the conjugate ionosphere by the CUTLASS and EISCAT radar. *Ann. Geophys.*, 19(10-12):1491–1508, 2001.
- [35] J. A. Wild, S. E. Milan, J. A. . Davies, S. W. H. Cowley, C. M. Carr and A. Balogh. Double Star, Cluster, and ground-based observations of magnetic reconnection during

- an interval of duskward oriented IMF: preliminary results. *Ann. Geophys.*, 23(8):2903, 2005.
- [36] T. K. Yeoman and D. M. Wright. ULF waves with drift resonance and drift-bounce resonance energy sources as observed in artificially-induced HF radar backscatter. *Ann. Geophys.*, 19(2):159–170, 2001.